High-contrast imaging polarimetry of exoplanets and circumstellar disks

Holstein, R.G. van

6 Circular polarimetric imaging at planetary system scales by hacking SPHERE-IRDIS: Full-Stokes observations of the asymmetric nebula surrounding VY CMa[1]

K. N. Strelow, D. A. Abbink, R. G. van Holstein, S. P. Bos, and F. Snik

Context. Measuring near-infrared circular polarization at high spatial resolution is a promising method to characterize the dust and magnetic fields in protoplanetary disks and around evolved stars, and could even shed light on the emergence of homochirality in biomolecules. However, current high-contrast imaging polarimeters such as SPHERE-IRDIS at the Very Large Telescope are not designed to measure circular polarization.

Aims. We develop the observing scheme, data-reduction methods, and analysis tools to measure circular polarization with SPHERE-IRDIS.

Methods. The image derotator (K-mirror) of SPHERE acts as an almost perfect quarter-wave retarder in the H- and K_s-bands. We devised an observing scheme that uses the derotator as polarization modulator to convert incident circular polarization into measurable linear polarization. We tested the technique with H-band observations of the red hypergiant VY CMa and its surrounding asymmetric nebula, and reduced the data using our model of the instrumental polarization effects of SPHERE-IRDIS.

Results. We find that the efficiency of measuring circular polarization is close to 100% and that the instrument-induced circular polarization is small (<0.1%) and well corrected for with the instrument model. The accuracy of our measurements is limited by the less-well-calibrated linear-to-circular polarimetric crosstalk produced by the telescope and SPHERE's first mirror. To more accurately constrain this crosstalk, we use the spatial variation of the linear polarization in the nebula of VY CMa to distinguish between real astrophysical circular polarization and crosstalk-induced signal. We find that the light from VY CMa in H-band is 4.07 ± 0.05% linearly polarized and 0.14 ± 0.04% circularly polarized, in agreement with the literature. These polarization signals most likely originate from a spatially unresolved, asymmetric circumstellar structure located close to the star that is optically thick or contains magnetically aligned dust grains. We also detect several so-far-unresolved features in the nebula surrounding VY CMa in linearly polarized light, but do not conclusively detect spatially resolved circular polarization.

Conclusions. In order to maximize the accuracy of future measurements, the instrumental

[1] *Author contributions:* As part of their BSc research project, KS and DA modeled the polarization modulation and instrumental polarization effects, performed the data reduction, calibrated the retardances of the UT and M4, and developed the data visualizations. RGvH devised and implemented the measurement technique at SPHERE-IRDIS, carried out the observations, supervised the BSc students, interpreted the measurements of VY CMa and its nebula, and led the writing. SB and FS co-supervised the BSc research project. FS suggested the new circular-polarization mode and developed the science case. All authors contributed to discussions during the research project and the writing.

crosstalk should be further calibrated by observing a face-on-viewed circumstellar disk. Our observing scheme enables the first measurements of spatially resolved circular polarization in protoplanetary disks and the nebulae around evolved stars.

6.1 Introduction

Measuring scattering-induced near-infrared (NIR) circular polarization at high spatial resolution can provide unique diagnostics for the characterization of the dusty environments of protoplanetary disks and the nebulae around evolved stars. Contrary to NIR linear polarization that can be produced by single scattering of unpolarized starlight, circular polarization is created through higher-order scattering processes that break mirror symmetry and is therefore not very common. In fact, disregarding the possibility of chiral scattering particles with a single handedness, the creation of circular polarization through scattering requires that symmetry is broken twice. Typically, a first scattering event creates linearly polarized light from essentially unpolarized starlight, after which this linear polarization is (partially) converted into circular polarization by a second interaction that mimics the effect of a retarder (e.g., a quarter-wave plate at $\pm 45^{\circ}$ to the incident linear polarization for perfect conversion).

The first mechanism to create circular polarization is multiple scattering of anisotropic radiation off spherical dust grains (i.e., multiple Mie scattering; Shafter & Jura, 1980; Bastien & Ménard, 1990). In this mechanism, the linearly polarized light created by scattering off dust grains is re-scattered by other grains, which, for favorable 3D scattering angles and dust geometries, produces circular polarization. The second mechanism to create circular polarization is scattering off elongated dust grains that are aligned to a large-scale magnetic field (Gledhill & McCall, 2000). In this case, the circular polarization results from a multiple-scattering scenario in which linearly polarized light that is created elsewhere is scattered off grains that are aligned at an oblique angle with respect to the incoming linear polarization. Alternatively, if the grains are aligned at an oblique angle with respect to the scattering plane, circular polarization can be created by a single scattering event that combines the creation of linear polarization and retardance. Whereas multiple Mie scattering yields relatively modest degrees of circular polarization of $\lesssim 1\%$, scattering by aligned grains can produce circular-polarization signals of tens of percent (Hough, 2006). The higher-order scattering mechanisms can also produce non-azimuthally oriented linear polarization, that is, linear polarization that is not oriented orthogonal to the direction toward the central star (e.g., Canovas et al., 2015). Therefore, measurements of both the linear and circular polarization in protoplanetary disks and the nebulae around evolved stars can yield strong constraints on the distribution of the scattering material, scattering asymmetries, dust properties (e.g., size, shape, and texture), and magnetic-field geometries.

Detecting circular polarization in protoplanetary disks is especially interesting because circular polarization may be responsible for the emergence of biological homochirality, which is one of the most fundamental properties of life (Bailey et al., 1998; Lucas et al., 2005; Modica et al., 2014; Patty et al., 2018; Avnir, 2021). Biology primarily uses one of two mirror-image versions (enantiomers) of complex molecules such as

amino acids and sugars (the building blocks of biological macromolecules such as DNA), whereas pure chemistry does not have such biases (Nelson et al., 2008). Homochirality may originate from an initially small enantiomeric imbalance in these molecules that is then amplified by specific (bio)chemical or physical processes (Bonner, 1991). Bailey et al. (1998) suggest that circularly polarized ultraviolet radiation can create an enantiomeric imbalance in the organic molecules in star-forming regions and protoplanetary disks through selective destruction of enantiomers, after which these organic molecules are delivered to forming planets and moons by impacting planetesimals and dust. Unfortunately, the ultraviolet radiation in these systems is difficult to observe because it is mostly obscured from our view by dust. However, Bailey et al. (1998) show that circular polarization at ultraviolet wavelengths can be created through the same higher-order scattering processes that produce NIR circular polarization. Large-scale and strong NIR circular polarization has been detected in many star-forming regions with wide-field imaging polarimetry (e.g., Chrysostomou et al., 1997; Bailey et al., 1998; Chrysostomou et al., 2000; Ménard et al., 2000; Buschermöhle et al., 2005; Kwon et al., 2013, 2014, 2018). However, to really show that circular polarization can contribute to the origin of homochirality on forming planets, we need to measure the NIR circular polarization in protoplanetary disks.

The seeing-limited instruments that have so far been used to measure NIR circular polarization cannot reach the high contrast and subarcsecond resolutions required to image protoplanetary disks and the nebulae around evolved stars. The adaptive-optics-assisted high-contrast imaging instrument SPHERE-IRDIS (Beuzit et al., 2019; Dohlen et al., 2008) at the Very Large Telescope has a well-established NIR dual-beam polarimetric imaging mode (de Boer et al., 2020; Chapter 2) that is very successful at imaging and characterizing circumstellar disks and (sub)stellar companions with a high spatial resolution in linearly polarized light (see e.g., Garufi et al., 2017; Avenhaus et al., 2018; Ginski et al., 2018; Chapter 5). Although SPHERE-IRDIS is not designed to measure circular polarization, in Chapter 2 it is suggested that the instrument can be made sensitive to circular polarization without changing its optical components. The Mueller matrix model of the instrumental polarization effects of the complete optical path of SPHERE-IRDIS shows that at some orientations the image derotator of SPHERE produces very strong circular-to-linear polarimetric crosstalk in the H- and K_s-bands. The derotator can therefore be used as polarization modulator to convert incident circular polarization into linear polarization that can be measured with the linear polarizers in IRDIS.

In this chapter, we present an observing scheme with SPHERE-IRDIS that uses the derotator as a polarization modulator to measure NIR circular polarization at subarcsecond resolution. We test the new observing scheme with linear- and circular-polarization measurements of the evolved star VY Canis Majoris (VY CMa) and its surrounding nebula. Using the Mueller matrix model of Chapter 2, we examine the efficiency of measuring circular polarization and quantify the circular polarization induced by the telescope and instrument. To reduce the data, we adapt the publicly available `IRDAP` (IRDIS Data reduction for Accurate Polarimetry) pipeline that uses the Mueller matrix model of Chapter 2 to correct observations for instrumental polarization effects with an absolute polarimetric accuracy of $\lesssim 0.1\%$ in the degree of polarization. Because the accuracy of our circular-polarization measurements turns out to be limited by the uncertainty

of the polarimetric crosstalk produced by the telescope and SPHERE's first mirror, we use the data of VY CMa itself to more accurately constrain this crosstalk.

Our test target VY CMa is an 8.2 Myr-old red hypergiant star with a mass of $17 \pm 8 M_{\odot}$ and an effective temperature of 3490 ± 90 K (Wittkowski et al., 2012; Zhang et al., 2012). The star is located at a distance of 1.17 ± 0.08 kpc and has a radius of $1420 \pm 120 R_{\odot}$, making it one of the largest stars known. VY CMa is surrounded by a nebula that is several arcseconds wide and comprises dusty clumps of ejecta that are asymmetrically distributed around the star (e.g., Monnier et al., 1999; Smith et al., 2001; Humphreys et al., 2007; Jones et al., 2007; Smith et al., 2009; Shenoy et al., 2013, 2015; O'Gorman et al., 2015; Scicluna et al., 2015). Linear-polarization measurements at visible and NIR wavelengths show that these clumps contain micron-sized dust grains (Scicluna et al., 2015) and suggest that some of these clumps are optically thick (Jones et al., 2007; Shenoy et al., 2015). As a result, it is possible that the light from these clumps scattered multiple times and is therefore circularly polarized. Gehrels (1972) and Serkowski (1973) detect NIR circular polarization from VY CMa through aperture polarimetry on the central source (0.4% in *I*-, 0.2% in *H*-, and 0.1% in *K*-band), but because these observations do not spatially resolve the nebula it is unclear where in the nebula this circular polarization originates.

The outline of this chapter is as follows. We describe the observing scheme to measure circular polarization in Sect. 6.2 and outline the test observations of VY CMa in Sect. 6.3. Subsequently, we investigate the instrumental polarization effects of the circular-polarization measurements in Sect. 6.4. Next, we present the data reduction in Sect. 6.5 and use the test data of VY CMa itself to further constrain the polarimetric crosstalk in Sect. 6.6. In Sect. 6.7 we present and discuss the measured linear and circular polarization of VY CMa and its nebula. Finally, we present conclusions in Sect. 6.8.

6.2 Observing scheme for measuring circular polarization

In this section, we describe the observing scheme we developed to measure circular polarization with SPHERE-IRDIS. We build on the efforts described in de Boer et al. (2020) and Chapter 2 and adopt the same definitions for the (optical components') orientation angles and the Stokes parameters. Of these Stokes parameters, I is the total intensity and positive and negative Q describe vertical (north-south) and horizontal (east-west) linear polarization. When looking into the beam of light, positive and negative U describe linear polarization oriented 45° counterclockwise and clockwise from positive Q, and positive and negative V describe circular polarization with clockwise and counterclockwise rotation. We refer to positive and negative V as right-handed and left-handed circular polarization, respectively. In Sect. 6.2.1 we summarize the optical path of SPHERE-IRDIS' polarimetric mode and the measurement of linear polarization. For a detailed description of the mode we refer to de Boer et al. (2020) and Chapter 2. In Sect. 6.2.2 we discuss the observing scheme to measure circular polarization.

6.2.1 SPHERE-IRDIS' polarimetric mode for linear polarimetry

A schematic overview of the optical path of SPHERE-IRDIS for polarimetric measurements is shown in Fig. 6.1. Light is collected by the primary mirror of the altazimuth-mounted Unit Telescope (UT) and is subsequently refocused by the secondary mirror (M2) that is suspended at the top of the telescope. The inclined tertiary mirror (M3) of the UT then reflects the light to the Nasmyth platform on which SPHERE is installed. Within SPHERE, the light is reflected off another inclined mirror (M4) and passes a rotatable half-wave plate (HWP) and the image derotator, which is a rotatable assembly of three mirrors (a K-mirror). In field-tracking mode, the derotator follows a rotation law that keeps the image in a fixed orientation on the detector (de Boer et al., 2020, Appendix A):

$$\theta_{\mathrm{der}} = \frac{1}{2}\,(-p + a + \eta) + n \cdot 180^{\circ}, \tag{6.1}$$

where θ_{der} is the derotator angle, p the parallactic angle, a the telescope altitude angle, η a user-defined image-position-angle offset, and n an integer that is determined by the control software. After the derotator, the light passes the mirrors of the adaptive optics system and the coronagraphs (not shown in Fig. 6.1). Subsequently, the light enters IRDIS and is split into two beams by a nonpolarizing beamsplitter and a mirror. The beams then pass a pair of linear polarizers with orthogonal transmission axes oriented in the vertical and horizontal directions, that is, in the directions perpendicular and parallel to the Nasmyth platform. Finally, the beams fall on the detector and create two adjacent (left and right) images of the orthogonal linear-polarization states.

During observations in field-tracking mode, the HWP keeps the linear polarization incident on the telescope in a fixed orientation with respect to the detector. In addition, the HWP acts as a modulator and selects the incident linear polarization to be measured. To this end, the HWP follows the rotation law (de Boer et al., 2020, Appendix A):

$$\theta_{\mathrm{HWP}} = -p + a + \frac{1}{2}\,(\eta + \gamma) + \theta^{\mathrm{s}}_{\mathrm{HWP}}, \tag{6.2}$$

where θ_{HWP} is the HWP angle, γ is an additional position angle offset (in general $\gamma = 0^{\circ}$), and $\theta^{\mathrm{s}}_{\mathrm{HWP}}$ is the HWP switch angle. In one HWP cycle, the HWP switch angle takes on values equal to 0° and 45° to measure incident Stokes Q and 22.5° and 67.5° to measure incident Stokes U.

For each HWP switch angle, we subtract the right image from the left image (the single difference) to obtain the Q^{+}-, Q^{-}-, U^{+}-, and U^{-}-images, respectively. We then compute images of Stokes Q and U from these images using the double difference as:

$$Q = \frac{1}{2}\,(Q^{+} - Q^{-})\,, \tag{6.3}$$

$$U = \frac{1}{2}\,(U^{+} - U^{-})\,. \tag{6.4}$$

We also add the left and right images for each HWP switch angle (the single sum) to obtain the $I_{Q^{+}}$-, $I_{Q^{-}}$-, $I_{U^{+}}$-, and $I_{U^{-}}$-images. Finally, we calculate the total-intensity I_{Q}-

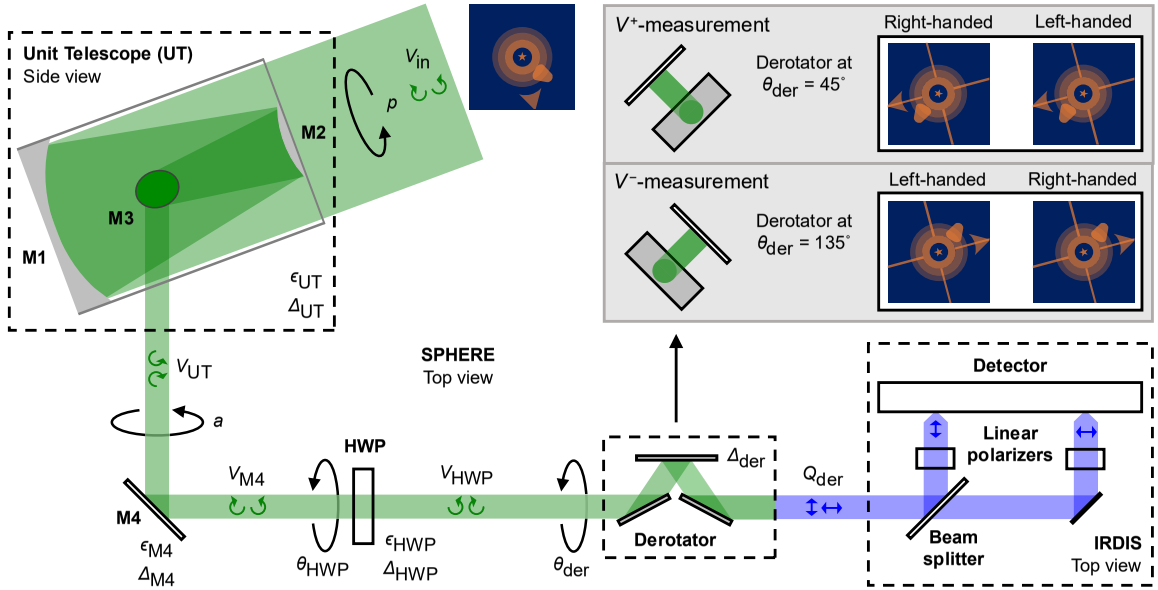

Figure 6.1: Overview of the optical path of the Unit Telescope (UT) and SPHERE-IRDIS, showing only the optical components relevant for polarimetric measurements, as well as a schematic depiction of the observing scheme to measure circular polarization. The names of the (groups of) components are indicated in boldface. The relevant diattenuations ϵ and retardances Δ of the components are shown as well. The black circular arrows indicate the parallactic angle p, the telescope altitude angle a, the half-wave plate (HWP) angle $\theta_{\rm HWP}$, and the derotator angle $\theta_{\rm der}$. Also indicated are the circularly polarized light (in green) incident on the telescope ($V_{\rm in}$) and downstream of the UT ($V_{\rm UT}$), M4 ($V_{\rm M4}$), and the HWP ($V_{\rm HWP}$) as well as the linearly polarized light (in blue) that the circularly polarized light is converted into downstream of the derotator ($Q_{\rm der}$). The gray area at the top right of the image shows the circular-polarization V^+- and V^--measurements taken with the derotator (viewed as looking along the incident beam) at angles equal to 45° and 135°, respectively. The gray area also shows the orientation of the images on the detector (images of VY CMa with the diffraction patterns of the M2 support structure; see Fig. 6.4, left) and the handedness of the circular polarization (right-handed or left-handed) corresponding to these measurements. Image adapted from Fig. 2.2.

and I_U-images from the double sum as:

$$I_Q = \frac{1}{2}\left(I_{Q^+} + I_{Q^-}\right), \tag{6.5}$$

$$I_U = \frac{1}{2}\left(I_{U^+} + I_{U^-}\right). \tag{6.6}$$

The polarimetric measurements with IRDIS are affected by the instrumental polarization effects of the optical components, which, as discussed in Chapter 2, consist of instrumental polarization (IP) and polarimetric crosstalk. IP is the polarization signal produced by the optical components and can make unpolarized sources appear to be polarized. For a single component, IP is a linear-polarization signal created by that component's diattenuation ϵ, that is, the difference between the reflectances or transmittances of the orthogonal linearly polarized components of the light. Crosstalk is the mixing of polarization states induced by the optical components. The crosstalk of a single component converts (part of the) incident linear polarization into circular polarization and vice versa. This crosstalk is produced by the component's retardance Δ, that is, the induced relative phase shift of the orthogonal linearly polarized components of the light. By computing the double difference (Eqs. (6.3) and (6.4)), the IP produced by the non-rotating components downstream of the HWP is removed because this IP manifests itself as transmission differences between the two beams falling on the detector. In addition, the double difference suppresses flat-field errors and uncorrected bad pixels (see e.g., Canovas et al., 2011). The crosstalk as well as the IP created by the UT and M4, which are located upstream of the HWP, need to be corrected for during the data reduction using the Mueller matrix model as implemented in IRDAP.

Even though the instrumental polarization effects can be corrected for in the data reduction, the crosstalk produced by the derotator can still significantly lower the attainable signal-to-noise ratio of field-tracking observations. From the Mueller matrix model of Chapter 2, we know that the derotator has a retardance of $\Delta_{\text{der}} = 99.32 \pm 0.06°$ in H-band and $\Delta_{\text{der}} = 84.13 \pm 0.05°$ in K_s-band, close to the 90° retardance of an ideal quarter-wave plate. This means that in these filters the derotator induces a nearly 90° relative phase shift between linearly polarized components incident parallel and perpendicular to the derotator's plane of incidence. In other words, the derotator can produce very strong linear-to-circular and circular-to-linear polarimetric crosstalk. For linear-polarization measurements, this crosstalk is no problem when θ_{der} is close to 0°, 90°, 180°, or 270°, that is, when the plane of incidence of the derotator is oriented nearly horizontal or vertical. However, when θ_{der} is close to 45°, 135°, 225°, or 315°, the derotator converts a large fraction of the incident linear polarization into circular polarization that cannot be distinguished with the linear polarizers of IRDIS. This results in a significant loss of polarimetric signal and therefore a large decrease of polarimetric efficiency, that is, the fraction of the linear polarization incident on the telescope that is actually measured. To ensure a high polarimetric efficiency, the derotator angle can be manually offset (i.e., by setting $\eta \neq 0°$ in Eq. (6.1)) such that θ_{der} is close to 0°, 90°, 180°, or 270° at the time of the observations (de Boer et al., 2020).

6.2.2 Observing scheme for measuring circular polarization

In our observing scheme to measure circular polarization, we turn the nearly quarter-wave retardance of the derotator in the H- and K_s-bands to our advantage by using the derotator as polarization modulator. A schematic depiction of the observing scheme is included in Fig. 6.1. We employ the field-tracking mode and take two measurements for which we deliberately offset $\theta_{\rm der}$ to values close to 45° and 135°. At these angles, the derotator converts almost all incident circular polarization into vertically and horizontally oriented linear polarization that can then be distinguished with IRDIS' linear polarizers.

In the data reduction, we subtract for each of the two measurements the right image from the left image to obtain the single-difference V^+- and V^--images, respectively. Contrary to the linear-polarization Q^+-, Q^--, U^+-, and U^--images, the different derotator angles used for the V^+- and V^--images result in the images being rotated approximately 180° with respect to each other (see Fig. 6.1). We therefore derotate (e.g., using spline interpolation) the V^+- and V^--images and use the resulting images to compute the image of Stokes V from the double difference as:

$$V = \frac{1}{2}\left(V^+ - V^-\right). \tag{6.7}$$

We also add the left and right images of the two measurements to obtain the single-sum I_{V^+}- and I_{V^-}-images. Similarly to the V^+- and V^--images, we first derotate the I_{V^+}- and I_{V^-}-images after which we compute the total-intensity I_V-image from the double sum as:

$$I_V = \frac{1}{2}\left(I_{V^+} + I_{V^-}\right). \tag{6.8}$$

Because the polarization state of the light is encoded in the positive and negative signals of the V^+- and V^--images, the derotation of these images does not alter the polarization information contained in them. Therefore, the overall IP created downstream of the HWP is still removed when computing the double difference. However, contrary to the linear-polarization measurements, each image point in the left and right images of the V^+- and V^--measurements are recorded on different pixels of the detector. As a result, the double difference does not suppress flat-field errors, uncorrected bad pixels, and any spatial variations of the IP of the left and right beams incident on the detector. These effects can decrease the attainable polarimetric accuracy when measuring the degree of polarization of point sources at the level of a few tenths of a percent (see Chapter 5). However, the effects are generally small and are therefore not expected to significantly affect measurements of the polarization of bright circumstellar structures or the halo of the central star. After computing the double difference, the measurements of circular polarization are, similar to linear-polarization measurements, still affected by the crosstalk as well as the IP created by the UT and M4. Therefore, also the circular-polarization measurements need to be corrected for the instrumental polarization effects during the data reduction using the Mueller matrix model.

6.3 Test observations of VY CMa

To test our observing scheme, we observed VY CMa, which is one of only a few stars that are visible from the Paranal Observatory and for which circular polarization has previously been detected in H-band (Serkowski, 1973). We performed the observations during the morning twilight on January 13, 2020. We used the H-band filter and the apodized Lyot coronagraph with a mask diameter of 185 mas (Carbillet et al., 2011; Guerri et al., 2011). Because VY CMa has a high brightness (0.44 mag in H-band) we used a neutral-density filter that reduces the flux tenfold. At the start of the observations, we took sky frames to enable the subtraction of the sky background and star-center frames to enable the determination of the position of the star behind the coronagraph. We then performed 12 measurements of circular polarization and four regular measurements of linear polarization. Each of these 16 measurements consisted of 15 integrations (NDIT) of 2 s (DIT) each, summing to a total on-source exposure time of 8 min. The atmospheric conditions were excellent with an average seeing and coherence time of 0.4″ and 6.9 ms, respectively. An overview of the relevant (component) angles of the measurements is shown in Table 6.1.

For both the linear-polarization and circular-polarization measurements we used standard `SPHERE_irdis_dpi_obs` observation templates. We performed the measurements of linear polarization using a single conventional HWP cycle with HWP switch angles equal to 0°, 45°, 22.5°, and 67.5° (setting `SEQ.IRDIS.POL.STOKES` to "QU" in the observation template). To ensure a high (linear) polarimetric efficiency, we used an image position angle offset of $\eta = 249°$ to set $\theta_{\text{der}} \approx 270°$. These linear-polarization measurements are indicated in Table 6.1 as the Q^+-, Q^--, U^+-, and U^--measurements.

For the measurements of circular polarization, we employed a series of templates that each use a partial HWP cycle with HWP switch angles equal to 0° and 45° (setting `SEQ.IRDIS.POL.STOKES` to "Q"). For this series of templates, we alternately used derotator image-position-angle offsets of $\eta = 159°$ and $\eta = 339°$ to obtain measurements with derotator angles $\theta_{\text{der}} \approx 45°$ and $\theta_{\text{der}} \approx 135°$, respectively. These circular-polarization measurements are displayed in Table 6.1 as the V^+- and V^--measurements. From this table, we see that for the same value of η the derotator angle can have two values 180° apart, that is, θ_{der} is sometimes close to 225° instead of 45°, or 315° instead of 135°. This is not a problem because these derotator angles are effectively equivalent and result in the same image orientation and circular-to-linear polarimetric crosstalk. The two possible values of the derotator angle result from the control software choosing the value of n in Eq. (6.1) such that the derotator rotates to the closest angle that gives the desired image orientation. Finally, because the values of θ_{der} are not exactly equal to 45°, 135°, 225°, and 315°, the images of the V^+- and V^--measurements are only approximately 180° rotated with respect to each other.

We note that the HWP, and therefore also switching the HWP, is not necessary for measurements of circular polarization. However, there exists no template for IRDIS' polarimetric mode that allows to remove the HWP or use less than two HWP switch angles. We therefore accept the limitations and in the data reduction simply compute the double-difference V-images from the V^+- and V^--images with the same HWP switch angle.

Table 6.1: Overview of the linear and circular-polarization measurements of VY CMa in H-band.

File	Stokes	η (°)	p (°)	a (°)	θ_{der} (°)	$\theta^{\mathrm{s}}_{\mathrm{HWP}}$ (°)
1	V^-	339	102.9	35.5	135.8	0
2	V^-	339	103.0	35.3	135.6	45
3	V^+	159	103.1	35.0	225.5	0
4	V^+	159	103.1	34.8	225.3	45
5	Q^+	249	103.2	34.6	270.1	0
6	Q^-	249	103.3	34.4	270.0	45
7	U^+	249	103.4	34.2	269.9	22.5
8	U^-	249	103.4	34.0	269.8	67.5
9	V^-	339	103.5	33.7	314.6	0
10	V^-	339	103.6	33.5	314.5	45
11	V^+	159	103.7	33.3	44.3	0
12	V^+	159	103.7	33.1	44.1	45
13	V^-	339	103.8	32.8	134.0	0
14	V^-	339	103.9	32.6	133.8	45
15	V^+	159	104.0	32.3	223.6	0
16	V^+	159	104.1	32.1	223.5	45

Notes. In the header of the table, Stokes shows the single difference Stokes parameter corresponding to the measurement, η is the user-defined image-position-angle offset of the derotator, p is the parallactic angle, a is the telescope altitude angle, θ_{der} is the derotator angle, and $\theta^{\mathrm{s}}_{\mathrm{HWP}}$ is the half-wave plate switch angle.

6.4 Instrumental polarization effects of circular-polarization measurements

To understand the performance of our observing scheme for measuring circular polarization and enable accurate reduction and interpretation of the measurements of VY CMa, we need to investigate how these measurements are affected by instrumental polarization effects. To this end, we use the Mueller matrix model of Chapter 2 to compute the instrumental polarization effects of observations of VY CMa in H-band. Although the exact magnitude of the effects differs for measurements in K_s-band or observations of targets with declinations other than that of VY CMa, the main conclusions we draw in this section remain the same. In Sect. 6.4.1 we outline the Mueller matrix model and the setup of our calculations. Subsequently, we investigate and explain the polarimetric efficiency, IP, and polarimetric crosstalk in Sects. 6.4.2, 6.4.3, and 6.4.4, respectively. Finally, we discuss the effect of the uncertainty of the retardance of the UT and M4 on the instrumental polarization effects in Sect. 6.4.5.

6.4.1 Mueller matrix model and setup of calculations

The Mueller matrix model mathematically describes the instrumental polarization effects of the complete optical system as a function of the parallactic, altitude, HWP, and derotator angles, and is described in detail in Chapter 2. The model uses three principal reference frames: the celestial reference frame, with positive Q aligned with the north-south direction on the sky; the telescope reference frame, which is rotated with respect to the celestial reference frame with the parallactic angle; and the instrument reference frame, which is rotated with respect to the telescope reference frame with the altitude angle and where positive Q is aligned with the vertical direction. The parameters of the model that are most relevant for our discussion are (see Fig. 6.1) the diattenuation of the UT (ϵ_{UT}; which is ideally completely due to M3), the retardances of the UT, M4, the HWP, and the derotator (Δ_{UT}, Δ_{M4}, Δ_{HWP}, and Δ_{der}), and, to a lesser extent, the diattenuations of M4 and the HWP (ϵ_{M4} and ϵ_{HWP}). The retardances of the UT (assumed to be completely due to M3) and M4 have been computed analytically from the Fresnel equations using the complex refractive indices of aluminum retrieved from Rakić et al. (1998); all other model parameters have been experimentally determined from measurements with SPHERE's internal light source and observations of unpolarized stars.

To compute the instrumental polarization effects of measurements of VY CMa, we simulate idealized double-difference measurements for the period of time during which VY CMa is seen above the horizon from the Paranal Observatory. To this end, we first define the Stokes vector describing the polarization state of the light incident on the telescope, that is, we define $\boldsymbol{S}_{\mathrm{in}} = [I_{\mathrm{in}}, Q_{\mathrm{in}}, U_{\mathrm{in}}, V_{\mathrm{in}}]^{\mathrm{T}}$, where I_{in}, Q_{in}, U_{in}, and V_{in} are the incident Stokes parameters in the celestial reference frame. Subsequently, we define a series of points in time and compute for each of them the parallactic angle and altitude angle. For each point in time we also define a pair of V^+- and V^--measurements where we set the derotator angles of all V^+-measurements equal to 45° and those of all V^--measurements equal to 135°. Next, we compute the derotator image-position-angle offsets η to reach those derotator angles from Eq. (6.1). Using the values of η, we then compute the corresponding HWP angles from Eq. (6.2), setting $\gamma = 0°$ and $\theta^{\mathrm{s}}_{\mathrm{HWP}} = 0°$, where the latter corresponds to the V^+- and V^--measurements with odd file numbers in Table 6.1 (the results only differ marginally for $\theta^{\mathrm{s}}_{\mathrm{HWP}} = 45°$). After that, we use the Mueller matrix model to compute for each pair of V^+- and V^--measurements the intensities reaching the left and right sides of the detector. From these intensities, we calculate the double-difference and double-sum intensities, after which we compute the measured normalized Stokes parameter v (i.e., the degree of circular polarization) as the ratio of these two values. For the period that VY CMa is visible, these calculations thus yield a series of values of v, which, for specific incident Stokes vectors, we can interpret as the polarimetric efficiency, IP, and crosstalk.

6.4.2 Polarimetric efficiency

In Sect. 6.2.1 we defined the polarimetric efficiency in terms of linear polarization. For circular-polarization measurements, we adapt the definition and define the polarimetric efficiency as the fraction of the circular polarization incident on the telescope that is actu-

ally measured. To calculate the polarimetric efficiency, we simulate the double-difference measurements for the case of 100% circularly polarized light incident on the telescope, that is, we set $\boldsymbol{S}_{\rm in} = [1, 0, 0, 1]^T$. The polarimetric efficiency is then equal to the values of v resulting from the computations.

The calculated polarimetric efficiency as a function of altitude angle for observations of VY CMa in H-band is shown by the green curve in Fig. 6.2 (top). From this curve, we see that the polarimetric efficiency varies between 94.0% and 99.5%. Because these values are very close to the ideal value of 100%, we conclude that our observing scheme is very efficient at measuring circular polarization. Figure 6.2 (top) also shows the polarimetric efficiency of the six actual circular-polarization measurements of VY CMa (green data points) as computed using the angles from Table 6.1. The small offsets of these data points with respect to the green curve are due to the parallactic and altitude angles not being equal for the actual V^+- and V^--measurements, the derotator angles deviating slightly from their ideal values of 45° (225°) and 135° (315°), and, for half of the measurements, the HWP switch angles being equal to 45° instead of 0°. Finally, we note that in K_s-band the polarimetric efficiency ranges between 97.0% and 98.2% and is therefore slightly higher than in H-band. This is as expected because the retardance of the derotator in K_s-band is closer to 90° than the retardance in H-band.

The polarimetric efficiency is primarily determined by the retardances of the UT, M4, the HWP, and the derotator. Writing out part of the Mueller matrix model, we can summarize the main effect of these retardances as:

$$\begin{aligned} &V_{\rm in} \rightarrow V_{\rm UT} \rightarrow V_{\rm M4} \rightarrow V_{\rm HWP} \rightarrow Q_{\rm der} = \\ &-\cos\Delta_{\rm UT}\cos\Delta_{\rm M4}\cos\Delta_{\rm HWP}\sin\Delta_{\rm der} = 96.6\% \text{ in } H\text{-band}, \end{aligned} \tag{6.9}$$

where the first line of the equation shows the conversions of a Stokes parameter incident on the telescope (in this case $V_{\rm in}$, in the celestial reference frame) into different Stokes parameters downstream of the UT (in the telescope reference frame), M4, the HWP, and the derotator (all in the instrument reference frame). All these Stokes parameters are shown in Fig. 6.1. The retardances of the UT, M4, and the HWP ($\Delta_{\rm UT} = \Delta_{\rm M4} = 175.0°$ and $\Delta_{\rm HWP} = 170.7° \pm 0.1°$ in H-band) are close to the ideal value of 180°. Apart from inducing a change of handedness, these components therefore effectively reflect or transmit the circular polarization incident on the telescope. Contrary to the retardances of the UT, M4, and the HWP, the retardance of the derotator ($\Delta_{\rm der} = 99.32° \pm 0.06°$ in H-band) is close to the 90° of an ideal quarter-wave plate. When placed at an angle of 45° or 135°, the derotator therefore produces strong crosstalk that almost completely converts the circular polarization downstream of the HWP, $V_{\rm HWP}$, into a linear-polarization signal, $Q_{\rm der}$. Because the transmission axes of IRDIS' linear polarizers are aligned with the directions of positive and negative $Q_{\rm der}$, this $Q_{\rm der}$-signal can be distinguished with the polarizers. Whereas for $\theta_{\rm der} = 45°$ (the V^+-measurement) the $Q_{\rm der}$-signal has the opposite sign of $V_{\rm HWP}$, for $\theta_{\rm der} = 135°$ (the V^--measurement) the $Q_{\rm der}$-signal has the same sign. As a result, the single differences computed from the V^+- and V^--measurements have opposite signs, enabling the computation of the final value of Stokes V from the double difference (see Eq. (6.7)).

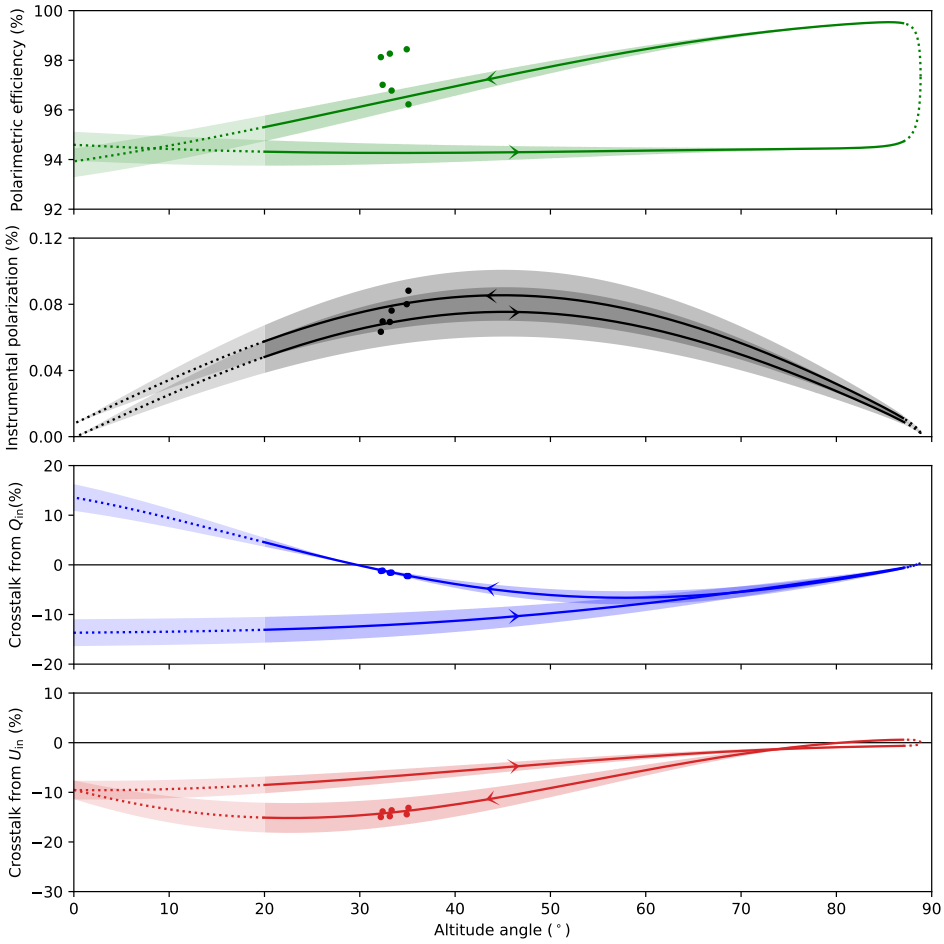

Figure 6.2: Polarimetric efficiency (*top*), instrumental polarization (*second row*), and crosstalk from incident Stokes Q (*third row*) and U (*bottom*) as a function of telescope altitude angle for circular-polarization measurements of VY CMa in H-band as computed from simulations of double-difference measurements with the Mueller matrix model of Chapter 2. The curves show the model values as calculated using ideal values of the parallactic, altitude, HWP, and derotator angles. In these curves, the arrowheads show the direction of increasing time and parallactic angle and the dotted parts indicate altitude angles that cannot actually be reached by the telescope. The data points show the model values of the six actual circular-polarization measurements of VY CMa as computed using the angles from Table 6.1. The data points deviate somewhat from the curves because the observations were performed with slightly different angles than the ideal angles used to compute the curves. The shaded areas indicate the uncertainty of the model values when assuming the retardances of the UT and M4 to have values between 174° and 176°.

The percentage on the right side of Eq. (6.9) is the polarimetric efficiency computed by substituting the H-band values of the model parameters (see Sect. 6.4.1) into the equation. This constant value of 96.6% is approximately equal to the average of the green curve in Fig. 6.2 (top). The small deviations from this value (i.e., those creating the loop in Fig. 6.2, top) are primarily due to the crosstalk of the HWP converting a small part of the incident circular polarization into linear polarization. Depending on the exact HWP angle (which in turn depends on the parallactic and altitude angle via Eqs. (6.1) and (6.2)), a fraction of this linear polarization is transmitted by the derotator (i.e., not converted to circular polarization) and contributes to the $Q_{\rm der}$-signal, thereby adding to the measured value of Stokes V.

6.4.3 Instrumental polarization

IP is the polarization signal produced by the optical components (see Sect. 6.2.1). For circular-polarization measurements, the IP refers specifically to the signal that contributes to the measurement of Stokes V. To compute the IP, we simulate the double-difference measurements for the case of completely unpolarized light incident on the telescope, that is, we set $\boldsymbol{S}_{\rm in} = [1,\ 0,\ 0,\ 0]^{\rm T}$. The IP is then equal to the values of v resulting from the calculations.

The computed IP as a function of altitude angle for observations of VY CMa in H-band is displayed with the black curve in Fig. 6.2 (second row). From the curve, it follows that the IP is (nearly) zero at an altitude angle of 0°, then increases to a maximum value of ∼0.08% at an altitude angle of 45°, and finally decreases toward zero again at an altitude angle of 90°. Compared to the maximum IP of more than 1% for linear-polarization measurements (Chapter 2), this IP is very small. Figure 6.2 (second row) also displays the IP of the six actual circular-polarization measurements of VY CMa (black data points) as calculated using the angles from Table 6.1. Similar to the polarimetric efficiency (see Sect. 6.4.2), the data points deviate somewhat with respect to the black curve because the observations were performed with slightly different angles than the ideal angles used to compute the curve. Finally, we note that in K_s-band the maximum IP is ∼0.04%, only half of that in H-band.

The IP is mainly produced by the combination of the diattenuation of the UT and the retardance of M4. Using the Mueller matrix model, we can write the principal process creating the IP as:

$$\begin{aligned} &I_{\rm in} \rightarrow Q_{\rm UT} \rightarrow V_{\rm M4} \rightarrow V_{\rm HWP} \rightarrow Q_{\rm der} = \\ &-\epsilon_{\rm UT} \sin(2a) \sin \Delta_{\rm M4} \cos \Delta_{\rm HWP} \sin \Delta_{\rm der} = \\ &\sin(2a) \cdot 0.077\% \text{ in } H\text{-band}, \end{aligned} \tag{6.10}$$

where in this case we take the total intensity as the Stokes parameter incident on the telescope. Initially, the diattenuation of the UT ($\epsilon_{\rm UT} = 0.0090 \pm 0.0001$ in H-band) produces a linear IP signal. Subsequently, a small part of this signal is converted into circular polarization by the crosstalk of M4. Besides the retardance of M4, the amount of circular polarization produced depends on the orientation of the linear polarization with respect

to M4, that is, it depends on the orientation of the telescope reference frame with respect to the instrument reference frame as defined by the altitude angle. The resulting circular polarization downstream of M4 is subsequently transmitted by the HWP (including a change of handedness) and converted to a measurable $Q_{\rm der}$-signal by the derotator (see Sect. 6.4.2). Interestingly, whereas for the IP of linear-polarization measurements the diattenuation of M4 ($\epsilon_{\rm M4} = 0.0092 \pm 0.0001$ in H-band) is equally important as the diattenuation of the UT (see Chapter 2), for circular-polarization measurements the diattenuation of M4 does not contribute at all.

The short expression on the right side of Eq. (6.10) is computed by substituting the values of the model parameters in H-band into the equation. This sinusoidal expression agrees well with the black curve in Fig. 6.2 (second row). However, from this figure we also see that for the same altitude angle the IP is slightly different for observations taken before or after passing the local meridian. These differences mainly result from the diattenuation of the HWP ($\epsilon_{\rm HWP} = -0.000297 \pm 7 \cdot 10^{-6}$ in H-band) that produces a small linear-polarization signal. Similar to the process described at the end of Sect. 6.4.2 and depending on the exact HWP angle, a small fraction of this signal is transmitted by the derotator and contributes to the $Q_{\rm der}$-signal, thus ending up in the measured value of Stokes V.

6.4.4 Crosstalk

As discussed in Sect. 6.2.1, polarimetric crosstalk is the mixing of polarization states induced by the optical components. For circular-polarization measurements, we are interested in the crosstalk that causes the linear polarization incident on the telescope to contribute to the measurement of Stokes V. We calculate the crosstalk by simulating the double-difference measurements for the cases of 100% Q- and U-polarized light incident on the telescope, that is, we perform the calculations twice, once with $\boldsymbol{S}_{\rm in} = [1,\ 1,\ 0,\ 0]^{\rm T}$ and once with $\boldsymbol{S}_{\rm in} = [1,\ 0,\ 1,\ 0]^{\rm T}$. In both cases the crosstalk is then equal to the values of v resulting from the computations.

The computed crosstalk for incident Q and U as a function of altitude angle for observations of VY CMa in H-band are shown in Fig. 6.2 (third row and bottom) with the blue and red curves, respectively. From these curves, it follows that the crosstalk is significant and can reach values of up to ∼15% at small altitude angles. At large altitude angles, the crosstalk reduces to a few percent. Figure 6.2 (third row and bottom) also shows the crosstalk of the six actual circular-polarization measurements of VY CMa (blue and red data points, respectively) as computed using the angles from Table 6.1. Similar to the polarimetric efficiency and IP (see Sects. 6.4.2 and 6.4.3), the data points show small deviations with respect to the curves because the angles from the observations are slightly different than the ideal angles used to calculate the curves. Finally, we note that the crosstalk in K_s-band has a maximum of ∼11%, somewhat lower than that in H-band.

The crosstalk is primarily produced by the retardances of the UT and M4. From the Mueller matrix model, we can derive the main process creating crosstalk from incident Q

as:

$$\begin{aligned} &Q_{\rm in}\rightarrow X_{\rm UT}\rightarrow V_{\rm M4}\rightarrow V_{\rm HWP}\rightarrow Q_{\rm der}\approx \\ &\quad[\sin(2p)\sin\Delta_{\rm UT}+\sin(2p-2a)\sin\Delta_{\rm M4}]\cos\Delta_{\rm HWP}\sin\Delta_{\rm der}= \\ &-[\sin(2p)+\sin(2p-2a)]\cdot 8.5\%\text{ in }H\text{-band}, \end{aligned} \tag{6.11}$$

where $X_{\rm UT}$ represents $Q_{\rm UT}$, $U_{\rm UT}$, and $V_{\rm UT}$ and we simplified the expression by assuming $\cos\Delta_{\rm UT}=\cos\Delta_{\rm M4}\approx -1$. Similarly, we can write the main process producing crosstalk from incident U as:

$$\begin{aligned} &U_{\rm in}\rightarrow X_{\rm UT}\rightarrow V_{\rm M4}\rightarrow V_{\rm HWP}\rightarrow Q_{\rm der}\approx \\ &-[\cos(2p)\sin\Delta_{\rm UT}+\cos(2p-2a)\sin\Delta_{\rm M4}]\cos\Delta_{\rm HWP}\sin\Delta_{\rm der}= \\ &\quad[\cos(2p)+\cos(2p-2a)]\cdot 8.5\%\text{ in }H\text{-band}. \end{aligned} \tag{6.12}$$

For both Q incident and U incident, the crosstalk is created following two distinct mechanisms. In the first mechanism, a small part of the incident Q- or U-polarization is converted to circular polarization by the crosstalk of the UT, after which this circular polarization is reflected by M4. In the second mechanism, the incident Q- or U-polarization is reflected by the UT, after which a fraction of the linear polarization is converted into circular polarization by the crosstalk of M4. Apart from the retardances of the UT and M4, the amount of circular polarization created in these two mechanisms depends on the orientation of the linear polarization in the telescope and instrument reference frames, respectively. Therefore, the crosstalk produced depends on the parallactic angle in the first mechanism and on both the parallactic and altitude angle in the second mechanism. In both mechanisms, the circular polarization created is subsequently transmitted by the HWP (including a change of handedness) and converted to a measurable $Q_{\rm der}$-signal by the derotator (see Sect. 6.4.2).

The expressions on the bottom lines of Eqs. (6.11) and (6.12) are calculated by substituting the H-band values of the model parameters into the equations. The two expressions are in good agreement with the blue and red curves in Fig. 6.2 (third row and bottom) and only show very small deviations that do not warrant further discussion. However, it is interesting to note that, even though the retardances of the HWP and the derotator are not ideal, these optical components do not cause additional crosstalk of the incident linear polarization (or the linear IP of the UT and M4) into the measurement of Stokes V. This is because the derotator as well as the HWP (following Eq. (6.2)) rotate 90° between the V^+- and V^--measurements. Due to the 90° rotations, the linear-polarization signals that are transmitted by the HWP-derotator combination and that contribute to the $Q_{\rm der}$-signal have the same sign in the V^+- and V^--measurements. As a result, these signals cancel when computing the double difference.

6.4.5 Effect of uncertainty of retardance of UT and M4

As discussed in Sects. 6.4.2–6.4.4, the polarimetric efficiency, IP, and crosstalk of circular-polarization measurements strongly depend on the retardances of the UT, M4, the HWP,

and the derotator. Of these retardances, the values of $\Delta_{\rm UT}$ and $\Delta_{\rm M4}$ have been computed from the Fresnel equations (see Sect. 6.4.1) and thus can differ significantly from the true values. As a result, the uncertainties of $\Delta_{\rm UT}$ and $\Delta_{\rm M4}$ can significantly decrease the achievable polarimetric accuracy after correcting for the instrumental polarization effects in the data reduction.

To examine the effect of the uncertainty of $\Delta_{\rm UT}$ and $\Delta_{\rm M4}$ on the instrumental polarization effects, we first make an estimate of the range of possible values of $\Delta_{\rm UT}$ and $\Delta_{\rm M4}$. To this end, we retrieve from several sources (Rakić, 1995; Rakić et al., 1998; McPeak et al., 2015; Ordal et al., 1988; Mathewson & Myers, 1971) the complex refractive indices of aluminum for the complete wavelength range of the H-band filter (1480–1770 nm). Assuming $\Delta_{\rm UT} = \Delta_{\rm M4}$, we then use the Fresnel equations to compute the retardance values from these refractive indices. From these calculations, we find $\Delta_{\rm UT}$ and $\Delta_{\rm M4}$ to have minimum and maximum values of approximately 174° and 176°, in agreement with the uncertainty due to the presence of oxide layers on aluminum mirrors (van Harten et al., 2009). Finally, we compute the polarimetric efficiency, IP, and crosstalk for $\Delta_{\rm UT} = \Delta_{\rm M4} = 174°$ and $\Delta_{\rm UT} = \Delta_{\rm M4} = 176°$ by repeating the calculations as described in Sects. 6.4.2–6.4.4 with these retardance values.

The resulting ranges of values for the polarimetric efficiency, IP, and crosstalk are displayed as shaded areas in Fig. 6.2. Figure 6.2 (top and second row) shows that the uncertainties in the polarimetric efficiency and IP are small. On the other hand, we see from Fig. 6.2 (third row and bottom) that the uncertainties in the crosstalk are significant and are largest for the points in time where the crosstalk is largest. Indeed, for the actual observations of VY CMa (data points in Fig. 6.2, third row and bottom) the large crosstalk from incident U (∼14%) is accompanied by an uncertainty of several percent. Whereas such large uncertainties in the crosstalk only marginally affect measurements of linear polarization, these uncertainties are very important for circular-polarization measurements. This is because the linear polarization in protoplanetary disks and the nebulae around evolved stars is expected to be generally much larger than the circular polarization. Therefore, if the value of 175.0° as used for $\Delta_{\rm UT}$ and $\Delta_{\rm M4}$ is slightly different from the true values, the part of the crosstalk that remains uncorrected in the data reduction can create large spurious signals in the images of Stokes V (see Sect. 6.6).

6.5 Data reduction

To reduce observations taken with our new observing scheme, we adapt the `IRDAP`[2] pipeline (version 1.2.3) that uses the Mueller matrix model to correct linear-polarization measurements for the instrumental polarization effects (Chapter 2). The most important adaptations concern the derotation of the images and the correction of the instrumental polarization effects. In this section, we describe the adapted data-reduction pipeline and apply it to the H-band observations of VY CMa.

The preprocessing of the raw files follows the exact same steps as used in the standard IRDAP. For each file, the pipeline subtracts the sky background, performs flat fielding, corrects for bad pixels, mean-combines the individual frames, and extracts the left

[2] https://irdap.readthedocs.io

and right images. Subsequently, it centers the left and right images using the star-center frames. For the observations of VY CMa, we exclude from the preprocessing the first three or four frames of the files that are taken after changing the image-position-angle offset (i.e., files 1, 3, 5, 9, 11, 13, and 15 in Table 6.1) because these frames show significant image smearing. The most likely cause of this smearing is that the rotation axis of the derotator is not exactly aligned with the position of the focal-plane mask of the coronagraph. As a result, the star moves away from the focal-plane mask with each large rotation of the derotator, after which the instrument needs several seconds to translate the image such that the star is placed behind the mask again.

After finishing the preprocessing, the pipeline subtracts the left and right images of each file, which in this case yields the single-difference Q^+-, Q^--, U^+-, U^--, V^+-, and V^--images. In addition, the pipeline adds the left and right images, thus creating the corresponding single-sum I_{Q^+}-, I_{Q^-}-, I_{U^+}-, I_{U^-}-, I_{V^+}-, and I_{V^-}-images. Contrary to the standard IRDAP, the pipeline then identifies the V^+-, V^-, I_{V^+}-, and I_{V^-}-images based on the derotator angle and derotates these images such that they have the same orientation with north upward. Finally, the pipeline computes cubes of double-difference Q-, U-, and V-images from Eqs. (6.3), (6.4), and (6.7) and cubes of double-sum I_Q-, I_U-, and I_V-images from Eqs. (6.5), (6.6), and (6.8).

As the next step, the pipeline uses the Mueller matrix model to correct the data for the instrumental polarization effects and computes the images of the Stokes parameters incident on the telescope. This model correction is very similar to that of the standard IRDAP because the Mueller matrix model simply depends on the (optical component) orientation angles and does not need to distinguish between the linear- and circular-polarization measurements. First, the pipeline subtracts the IP from each double-difference image. To this end, it scales the corresponding double-sum image with the computed IP and subtracts the resulting image from the double-difference image. Subsequently, the pipeline derotates the cubes of IP-subtracted Q- and U-images as well as the cubes of I_Q- and I_U-images such that north is upward (the IP-subtracted V-images and the I_V-images are already derotated). Next, the pipeline sets up a system of equations that describes for each derotated, IP-subtracted double-difference Q-, U-, or V-image the contribution of the crosstalk or transmission from incident Q, U, and V. The pipeline then computes the three images of incident Q, U, and V by solving, for every pixel individually, the system of equations using linear least squares (there are more than three measurements). The standard IRDAP differs from this in that it assumes the incident V to be zero and therefore solves the system of equations only for incident Q and U. Finally, the pipeline computes the three final I_Q-, I_U-, and I_V-images as the means of the cubes of derotated I_Q-, I_U-, and I_V-images, respectively.

From the three I_Q-, I_U-, and I_V-images, the pipeline subsequently computes the final total-intensity image by computing the mean of these images. Using the model-corrected Q- and U-images and following the definitions of de Boer et al. (2020), the pipeline also computes images of Q_ϕ and U_ϕ. In these images, positive and negative Q_ϕ show the linear polarization in the azimuthal and radial directions (i.e., orthogonal and parallel to the direction toward the central star), respectively, and positive and negative U_ϕ show the linear polarization at ±45° from these directions. Finally, the pipeline computes an image

of the linearly polarized intensity, PI_{L}, as:

$$PI_{\mathrm{L}} = \sqrt{Q^2 + U^2}, \tag{6.13}$$

and an image of the angle of linear polarization, χ, as:

$$\chi = \frac{1}{2} \arctan\left(\frac{U}{Q}\right). \tag{6.14}$$

The final polarization images contain halos of polarized starlight that originate from interstellar dust and/or spatially unresolved circumstellar material located close to the star. In Fig. 6.3, which shows the central part of the linearly polarized intensity image of VY CMa, the halo is primarily visible as a star-centered ring (the adaptive-optics residuals) and four lines emanating from the center of the image (the diffraction patterns of the M2 support structure). With the pipeline we can determine the stellar polarization from the I_Q-, I_U-, I_V-, and model-corrected Q-, U-, and V-images by summing the flux in these images in a region that only contains light from the stellar halo and no signal from spatially resolved circumstellar material. From the summed fluxes, the pipeline then computes the normalized Stokes parameters of the stellar polarization as $q = Q/I_Q$, $u = U/I_U$, and $v = U/I_U$. For the data set of VY CMa, we select the region indicated with the dotted lines in Fig. 6.3. The measured values of q, u, and v do not significantly change when varying the size of the selected region, suggesting that the region indeed does not contain signal from circumstellar material. Subsequently, the pipeline determines the uncertainty of the measured stellar polarization. For the measurement of v, the pipeline solves the system of equations describing the crosstalk for each V-measurement separately, measures the stellar polarization from the resulting images, and computes the standard error of the mean over the measured values. Because we have taken only one HWP cycle to measure Q and U, the pipeline computes the uncertainty of q and u as the accuracy of the Mueller matrix model with which the data is corrected (see Chapter 2).

Finally, the pipeline creates an additional set of images with the stellar polarization subtracted by scaling the I_Q-, I_U-, and I_V-images with the measured stellar q, u, and v and subtracting the resulting images from the model-corrected Q-, U-, and V-images. In the remainder of this chapter we only consider the images with the stellar polarization subtracted. The final images of the total intensity as well as of the linearly polarized intensity and angle of linear polarization of VY CMa in H-band are shown in Fig. 6.4. In addition, the final Q-, U-, Q_ϕ−, and U_ϕ-images are shown in Fig. 6.8. Because the star-centered ring of the adaptive-optics residuals is not visible in the polarization images, we conclude that the stellar polarization is overall well subtracted. Indeed, when subtracting polarization signals that are slightly larger or smaller than the measured stellar q, u, and v, the ring of the adaptive-optics residuals becomes visible in the images with overall positive or negative signal. Still, spurious signals due to diffraction by the M2 support structure, the spiders of the coronagraph Lyot stop, and defective actuators of the deformable mirror of the adaptive-optics system (Cantalloube et al., 2019) remain (slightly) visible in the polarization images, but this is because the diffraction features produced by these components rotate during observations in field-tracking mode.

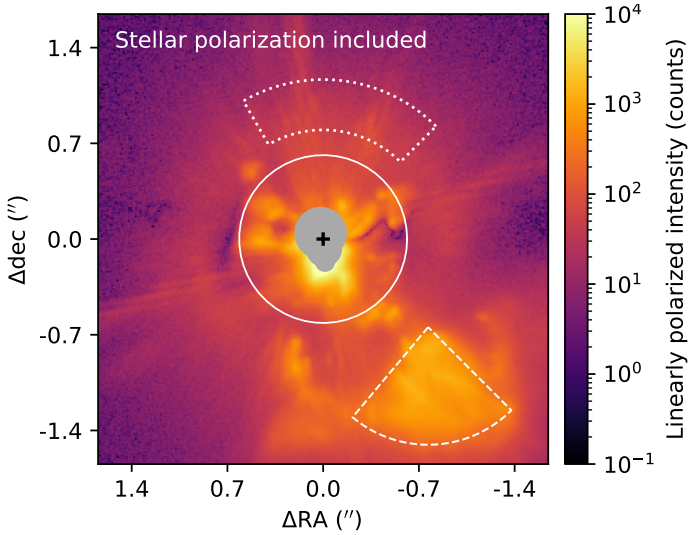

Figure 6.3: Central part of the linearly polarized intensity image of VY CMa in *H*-band before subtracting the stellar polarization. The three white shapes indicate the region used to measure the stellar polarization (dotted lines, Sect. 6.5) and the regions we denote the inner structure (solid line) and the southwest (SW) clump (dashed lines, Sect. 6.6). The position of the star is marked with the black plus sign. The gray area around this plus sign masks the region that is obscured by the focal-plane mask of the coronagraph and that contains saturated pixels and pixels with values in the nonlinear regime of the detector.

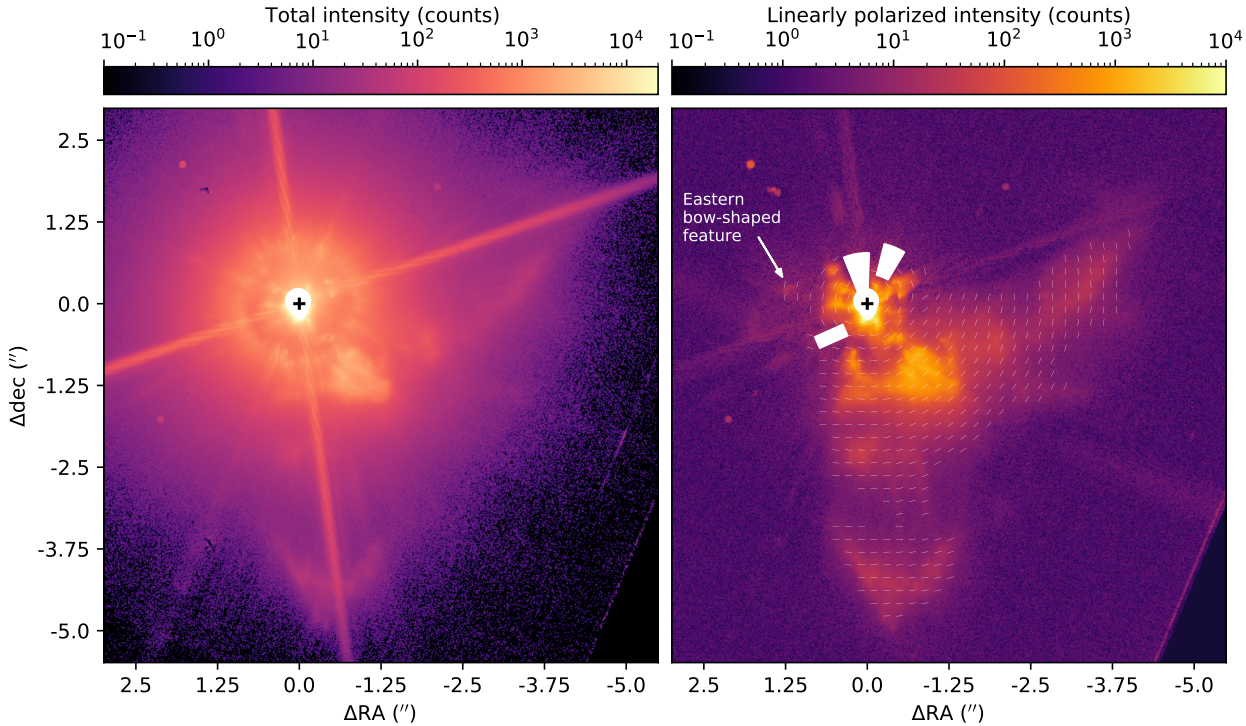

Figure 6.4: Images of the total intensity (*left*) as well as the linearly polarized intensity and angle of linear polarization after subtracting the stellar polarization (*right*) of VY CMa in *H*-band. The angle of linear polarization is indicated by white lines of arbitrary and constant length and is only shown where the average linearly polarized intensity in bins of 16×16 pixels is larger than 5 counts. The position of the star is marked with the black plus signs. The white areas around these plus signs mask the region that is obscured by the focal-plane mask of the coronagraph and that contains saturated pixels and pixels with values in the nonlinear regime of the detector. In the linearly polarized intensity image, several bright spurious features due to diffraction by the M2 support structure, Lyot stop, and deformable mirror are masked as well.

6.6 Calibration of crosstalk from data of VY CMa

As discussed in Sect. 6.4.5, the retardances of the UT and M4, $\Delta_{\rm UT}$ and $\Delta_{\rm M4}$, are relatively uncertain and therefore cause large uncertainties in the polarimetric crosstalk of circular-polarization measurements. As a result, it is not unlikely that part of the crosstalk from incident linear polarization remains uncorrected after the data reduction, thereby creating spurious signals in the image of Stokes V. In Sect. 6.6.1, we investigate whether the model-corrected V-image of VY CMa in H-band contains spurious signals. Subsequently, in Sect. 6.6.2, we use the data itself to constrain the H-band values of $\Delta_{\rm UT}$ and $\Delta_{\rm M4}$ that result in the best correction of the crosstalk.

6.6.1 Identification of spurious signals due to uncorrected crosstalk

To determine whether a model-corrected V-image contains spurious signals, we can examine the variation of the V-signals with time and position in the image. Whereas spurious V-signals vary with the parallactic and altitude angle as well as with the spatial distribution of incident Q- and U-signals (see Eqs. (6.11) and (6.12)), real incident V-signals are independent of these variables. Because the observations of VY CMa have very little variation in the parallactic and altitude angle (see Table 6.1), we need to rely on the spatial distribution of the incident Q- and U-signals (see Fig. 6.8, top) for the identification of spurious signals.

We can write the dependence of the spurious V-signals on the incident Q- and U-signals as:

$$V_{\rm CT} = (Q{\rightarrow}V) \cdot Q_{\rm in} + (U{\rightarrow}V) \cdot U_{\rm in}, \tag{6.15}$$

where $V_{\rm CT}$ is the spurious V-signal due to uncorrected crosstalk and $(Q{\rightarrow}V)$ and $(U{\rightarrow}V)$ are the parts of the crosstalk that remain uncorrected after the data reduction. We can rewrite Eq. (6.15) in terms of the linearly polarized intensity $PI_{\rm L}$ (Eq. (6.13)) and the angle of linear polarization χ (Eq. (6.14)). Substituting $Q_{\rm in} = PI_{\rm L}\cos(2\chi)$ and $U_{\rm in} = PI_{\rm L}\sin(2\chi)$ into Eq. (6.15) and rearranging, we obtain:

$$\frac{V_{\rm CT}}{PI_{\rm L}} = (Q{\rightarrow}V) \cdot \cos(2\chi) + (U{\rightarrow}V) \cdot \sin(2\chi). \tag{6.16}$$

This equation shows that when we compute an image of the ratio of Stokes V to the linearly polarized intensity, $V/PI_{\rm L}$, we can identify spurious signals from their variation with the angle of linear polarization. Figure 6.2 (third row and bottom) shows that for the observations of VY CMa the uncertainty of the crosstalk from incident U is much larger than that of the crosstalk from incident Q. As a result, the effect of $(U{\rightarrow}V)$ dominates over that of $(Q{\rightarrow}V)$ and we expect $V/PI_{\rm L}$ to vary with approximately $\sin(2\chi)$ if the V-signal is caused by uncorrected crosstalk. We should be able to identify such a sinusoidal signal in the data of VY CMa because in Fig. 6.4 (right) the angle of linear polarization covers the full range from 0° to 180°. Finally, we expect any spurious signal in the $V/PI_{\rm L}$-image to resemble a scaled version of the U-image (see Fig. 6.8, top right), either with the same or the opposite sign (see Eq. (6.15)).

To demonstrate that we can truly identify spurious V-signals from $V/PI_{\rm L}$-images, we repeat the data reduction as described in Sect. 6.5, but this time we set $\Delta_{\rm UT}$ and $\Delta_{\rm M4}$ to

the ideal value of 180° in the Mueller matrix model. In this way, the model-corrected V-image is not corrected for the crosstalk of the UT and M4 and therefore certainly contains spurious signal. After performing the data reduction, we bin the resulting V-, $PI_{\rm L}$-, and χ-images in bins of 2×2 pixels and compute the image of $V/PI_{\rm L}$. Subsequently, we create a scatter plot of the bins of $V/PI_{\rm L}$ as a function of χ. Because the ratio $V/PI_{\rm L}$ can become very noisy, we use only those bins for which both V and $PI_{\rm L}$ exceed 10 counts and for which $-0.5 \leq V/PI_{\rm L} \leq 0.5$. The resulting scatter plot and $V/PI_{\rm L}$-image are shown in Fig. 6.5 (top). The scatter plot exhibits a sinusoidal pattern and the $V/PI_{\rm L}$-image resembles the U-image of Fig. 6.8 (top right) with opposite sign. We therefore conclude that for the reduction with $\Delta_{\rm UT} = \Delta_{\rm M4} = 180°$ the V-signal is spurious, as expected.

Finally, we investigate whether the V-image of the original reduction of Sect. 6.5, with $\Delta_{\rm UT} = \Delta_{\rm M4} = 175.0°$, contains spurious signals. To this end, we perform the same analysis and show the results in Fig. 6.5 (center). In this case, the scatter plot exhibits only a slight hint of a sinusoidal pattern. However, the $V/PI_{\rm L}$-image quite clearly resembles the U-image of Fig. 6.8 (top right), although with much lower values of $V/PI_{\rm L}$ than in Fig. 6.5 (top). We thus conclude that the images of the original reduction contain some spurious signals due to uncorrected crosstalk, although much less than the images of the reduction with $\Delta_{\rm UT} = \Delta_{\rm M4} = 180.0°$.

6.6.2 Constraining retardance of UT and M4 from data

If we would reduce the data of VY CMa with the true values of $\Delta_{\rm UT}$ and $\Delta_{\rm M4}$, the $V/PI_{\rm L}$-image should ideally only show the real incident V-signal (if present) and no signals resembling the U-image of Fig. 6.8 (top right). To constrain the true value of $\Delta_{\rm UT}$ and $\Delta_{\rm M4}$ in H-band, we perform a series of data reductions in which we vary $\Delta_{\rm UT}$ and $\Delta_{\rm M4}$ from 170° to 180° in steps of 0.1°. In these reductions, we assume that $\Delta_{\rm UT} = \Delta_{\rm M4}$ because the observations of VY CMa do not have sufficient variation in parallactic and altitude angle to distinguish the two retardances. However, it is not unlikely that $\Delta_{\rm UT}$ and $\Delta_{\rm M4}$ are truly (nearly) equal because the measured diattenuations of the UT and M4 in H-band are very similar (see Sect. 6.4.3). After performing all the reductions, we compute the $V/PI_{\rm L}$-images and identify by eye the reductions with the least spurious signal.

A gallery of $V/PI_{\rm L}$-images for retardances between 170.5° and 180° in steps of 0.5° is shown in Fig. 6.9. Most images in this figure resemble a scaled version of the U-image of Fig. 6.8 (top right) and thus contain spurious signal. For retardances from 170.5° to 172.5°, the spurious signals have the same sign as the U-image, whereas for retardances from 174.5° to 180° the sign is opposite. Because the sign of the crosstalk from incident U is negative (see Fig. 6.2, bottom), the crosstalk is overcorrected for retardances from 170.5° to 172.5° and undercorrected for retardances from 174.5° to 180°. For retardances between 172.5° and 174.5°, the images in Fig. 6.9 exhibit less resemblance to the U-image and thus contain little spurious signal. The true H-band value of $\Delta_{\rm UT}$ and $\Delta_{\rm M4}$ therefore most likely lies between 172.5° and 174.5°.

To more quantitatively constrain the true value of $\Delta_{\rm UT}$ and $\Delta_{\rm M4}$, we compute for each reduction over some specified region the sum of squared normalized Stokes v-signal, which we denote $|v|^2$. For the computation of $|v|^2$, we first square the I_V- and model-corrected V-images. Subsequently, we sum the flux over the specified region in the re-

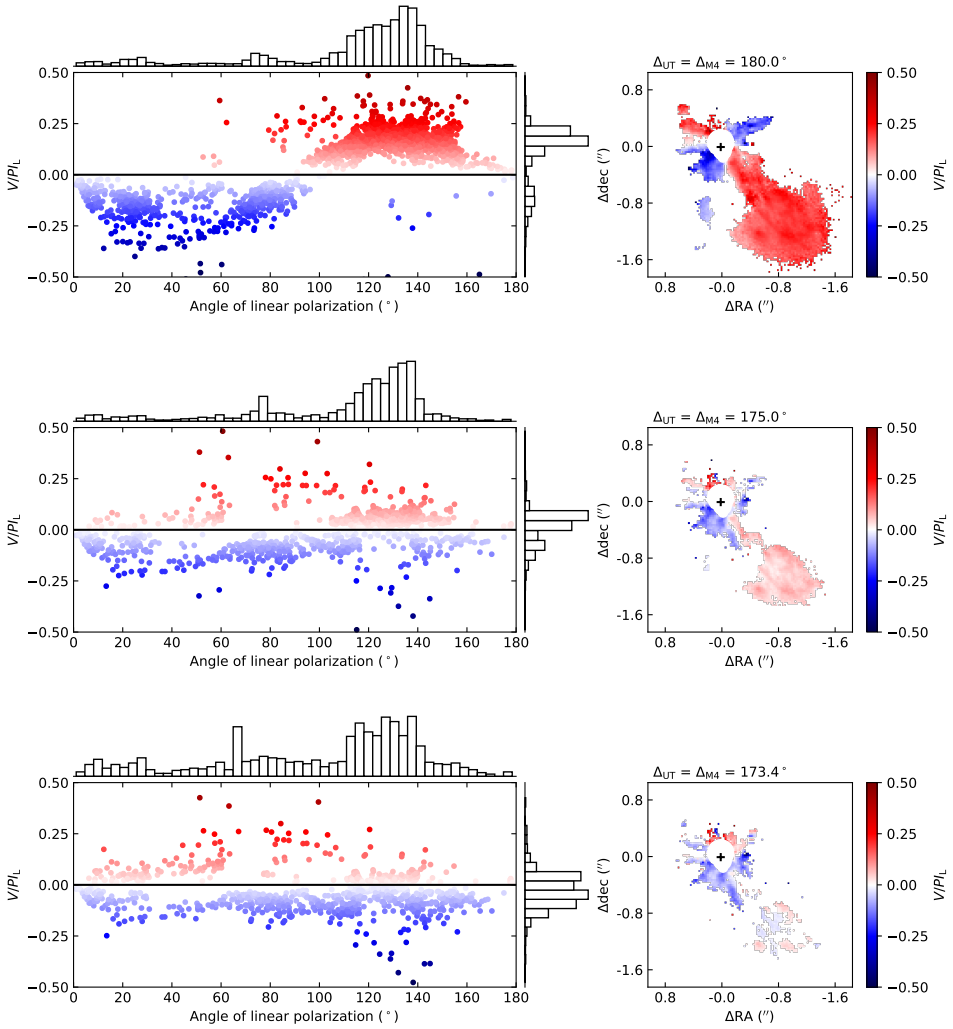

Figure 6.5: Scatter plots of the ratio of circular polarization to linearly polarized intensity $V/PI_{\rm L}$ as a function of angle of linear polarization χ (*left column*) and the corresponding images of $V/PI_{\rm L}$ (*right column*) for reductions of the H-band data of VY CMa using retardances of both the UT and M4 equal to 180° (*top*), 175° (*center*) and 173.4° (*bottom*). The data points in the scatter plots correspond to bins of 2×2 pixels in the images for which both V and $PI_{\rm L}$ exceed 10 counts and for which $-0.5 \leq V/PI_{\rm L} \leq 0.5$. The histograms on the top and right sides of the scatter plots show the distributions of the data points as a function of χ and $V/PI_{\rm L}$. The position of the star is marked with the black plus signs in the images. The white areas around these plus signs mask the region that is obscured by the focal-plane mask of the coronagraph and that contains saturated pixels and pixels with values in the nonlinear regime of the detector.

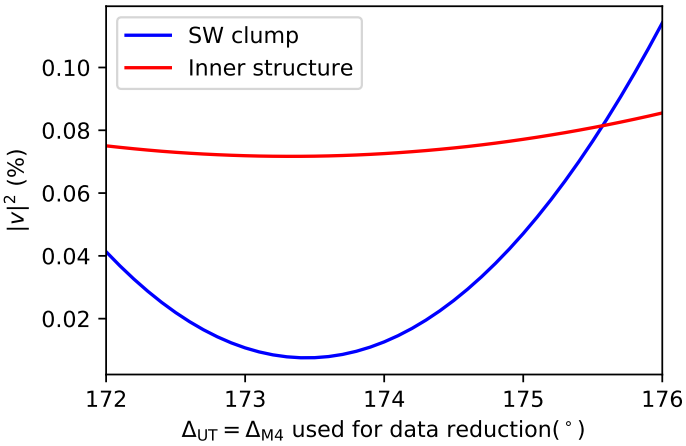

Figure 6.6: Sum of squared normalized Stokes v-signal, $|v|^2$, computed over the southwest (SW) clump and the inner structure as a function of the retardance of the UT and M4 used in the data reduction. The regions we denote the SW clump and inner structure are shown in Fig. 6.3.

sulting V^2- and I_V^2-images and compute $|v|^2$ as the ratio of the summed fluxes. The value of $|v|^2$ thus quantifies the total amount of (positive and negative) circular-polarization signal present in the specified region. We compute $|v|^2$ over the two brightest regions of the nebula of VY CMa that we resolve: the inner structure of circumstellar material close to the star and the clump to the southwest (SW) of star. These regions, which we denote the inner structure and the SW clump, are indicated in Fig. 6.3.

The $|v|^2$-values of the inner structure and the SW clump for reductions with retardances between 172° and 176° are shown in Fig. 6.6. From this figure, we see that the $|v|^2$-values of both regions reach a minimum for the reduction with $\Delta_{UT} = \Delta_{M4} = 173.4°$, suggesting that with this retardance the crosstalk is best corrected. The scatter plot and V/PI_L-image for the reduction with $\Delta_{UT} = \Delta_{M4} = 173.4°$ are shown in Fig. 6.5 (bottom). From this figure, the crosstalk indeed seems to be well corrected because the scatter plot does not exhibit a sinusoidal pattern and the V/PI_L-image shows only a slight resemblance to the U-image. However, significant signal is still visible close to the star, which is also reflected by the nonzero minimum of $|v|^2$ for the inner structure in Fig. 6.6. A large fraction of this signal is most likely spurious in nature and results from imperfect centering of the star behind the focal-plane mask of the coronagraph in combination with the rotations of the images; the diffraction patterns of the M2 support structure, Lyot stop, and deformable mirror; imperfect relative centering of the left and right images; the speckle field changing in time; and image motion during the observations. Such spurious structures are also consistently visible in images of regular linear-polarization measurements (see e.g., Chapter 4). Contrary to the inner structure, the SW clump contains only very small positive and negative signals in the V/PI_L-image of Fig. 6.5 (bottom). These signals almost completely cancel each other out, resulting in a nearly zero minimum of $|v|^2$ for the SW clump in Fig 6.6. This very low minimum may suggest that the crosstalk is almost completely

corrected. However, the range of angles of linear polarization in the SW clump is limited (see Fig. 6.4, right) and so the U-signal is locally very uniform (see Fig. 6.8, top right). Therefore, we cannot exclude the possibility that a real incident V-signal at the location of the SW clump cancels out a spurious V-signal due to uncorrected crosstalk from incident U. It is unfortunate that the only sufficiently bright region at a large separation from the star has a strong U-signal and that we took the observations at a time when the uncertainty in crosstalk from incident U is large. We conclude that we cannot be completely certain that for $\Delta_{\mathrm{UT}} = \Delta_{\mathrm{M4}} = 173.4°$ the crosstalk is best corrected. Nevertheless, under the assumption that there is no real incident V-signal in the SW clump, we conclude that the most likely value of Δ_{UT} and Δ_{M4} in H-band is 173.4°.

6.7 Linear and circular polarization of VY CMa and its nebula

Now that we have determined the more accurate value of 173.4° for Δ_{UT} and Δ_{M4} in H-band, we perform a final reduction of our measurements of VY CMa using this value. Whereas for this final reduction the image of Stokes V differs from the image obtained in the original reduction (see Sect. 6.6), the linear-polarization images exhibit no significant differences. In this section, we present and briefly discuss the resulting images and measurements. Our measurements, especially when combined with the polarimetric images in V- and I-band from Scicluna et al. (2015), can in principle be used for a detailed quantitative study of grain-size distributions, optical depths, and scattering geometries, but we consider such a detailed analysis beyond the scope of this chapter. In Sect. 6.7.1, we analyze the measured linear and circular stellar polarization and compare these measurements to measurements of VY CMa from the literature. Subsequently, in Sect. 6.7.2, we examine the spatially resolved linear and circular polarization of the nebula of VY CMa.

6.7.1 Spatially unresolved stellar polarization

As discussed in Sect. 6.5, we have measured the stellar polarization of VY CMa, expressed in terms of the normalized Stokes parameters q, u, and v, from the halo of polarized starlight visible in the final images. For the linear polarization of the star, we measure $q = -3.99 \pm 0.05\%$ and $u = 0.80 \pm 0.04\%$. These values translate to a degree of linear polarization, $P_{\mathrm{L}} = \sqrt{(q^2 + u^2)}$, equal to $P_{\mathrm{L}} = 4.07 \pm 0.05\%$ and an angle of linear polarization (see Eq. (6.14)) of $\chi = 84.3 \pm 0.3°$, where we have propagated the uncertainties using a Monte Carlo calculation and assuming Gaussian statistics. For the circular polarization, we measure $v = 0.14 \pm 0.04\%$, corresponding to right-handed circular polarization in our definitions (see Sect. 6.2). We also measure the stellar q, u, and v from reductions with Δ_{UT} and Δ_{M4} ranging from 172.5° to 174.5° and find that the variations in the measured normalized Stokes parameters are within the quoted uncertainties. This is also the case for the measurement of v because the starlight is predominantly polarized in q and the uncertainty of the crosstalk from incident Q is very small at the time of the observations (see Fig. 6.2, third row).

The measurements of the stellar q and u can contain a contribution from interstellar polarization. This interstellar polarization is almost exclusively linear and results from dichroic absorption (diattenuation) by elongated dust grains that are aligned with the magnetic field in the interstellar medium. To estimate the interstellar polarization, we compare our measurements to the known linear polarization of HD 58011, a background star located 15′ from VY CMa at a distance of ∼4 kpc (Bailer-Jones et al., 2018). From the catalog by Klare et al. (1972), we find that HD 58011 has a degree of linear polarization of $P_{\rm L} = 0.36 \pm 0.05\%$ in the spectral range from approximately 370 to 490 nm. We convert this degree of linear polarization to H-band using Serkowski's law of interstellar polarization (Serkowski et al., 1975; Whittet et al., 1992). Assuming that the degree of linear polarization is maximum at a wavelength of 590 nm, which is the average value for the 105 stars observed by Whittet et al. (1992), we find a degree of linear polarization of ∼0.1% in H-band. This degree of linear polarization of ∼0.1% for the interstellar polarization is negligible compared to the stellar q and u that we measure. We therefore conclude that the measured linear polarization of VY CMa, as well as the circular polarization, most likely originate from spatially unresolved circumstellar material located close to the star.

From aperture-masking interferometry with the 10-m Keck telescope, Monnier et al. (1999) show that the NIR flux within 0.1″ around VY CMa is dominated by an asymmetric structure with a projected major axis of ∼170° (east of north) located south of the star. Assuming single scattering only, such a structure would create an integrated polarization signal with an angle of linear polarization of ∼80°, in close agreement with our measured $\chi = 84.3 \pm 0.3°$. Because we also detect circular polarization, this inner circumstellar material likely causes some multiple scattering due to being optically thick and/or contains magnetically aligned dust grains. The latter is plausible because there is observational evidence for a magnetic field throughout the nebula of VY CMa (Humphreys et al., 2007).

The linear and circular polarization of VY CMa in H-band have been measured before from aperture polarimetry on seeing-limited observations by (among others) Serkowski (1973), Maihara et al. (1976), and Takami et al. (1992). Contrary to our measurements of the stellar polarization, which only contain the contributions from the innermost regions around the star, the measurements from the literature encompass the complete nebula. Before comparing our results with those from the literature, we therefore need to check that the parts of the nebula that are excluded from our measurements of stellar polarization (i.e., the parts we spatially resolve in the images) do not significantly contribute to the measurements from the literature. To this end, we use the IRDIS exposure-time calculator[3] to estimate the peak flux of the non-coronagraphic stellar point-spread function (PSF). Subsequently, we determine the peak fluxes of the SW clump and the non-saturated parts of the inner structure in the total-intensity image (see Fig. 6.4, left). Dividing the resulting values by the peak flux of the star, we find that the SW clump and the inner structure, which are the brightest regions in our images, have contrasts of $\sim 10^{-4}$ and $\sim 4 \cdot 10^{-3}$. We conclude that the circumstellar material we spatially resolve in our images does not significantly contribute to the measurements from the literature and that we can thus compare the measurements.

[3] https://www.eso.org/observing/etc/bin/gen/form?INS.NAME=SPHERE+INS.MODE=IRDIS

From H-band observations of VY CMa, Serkowski (1973) measured $P_L = 5 \pm 0.1\%$ and $\chi = 75°$ for the linear polarization and $v = 0.24 \pm 0.05\%$ (right-handed) for the circular polarization, which both agree reasonably well with our measurements of the stellar polarization. However, similar measurements of the linear polarization by Maihara et al. (1976) and Takami et al. (1992) yielded $P_L = 2.3\%$ and $\chi = 85°$, and $P_L = 8.3\%$ and $\chi = 98°$, respectively. Therefore, the degree of linear polarization, and possibly also the degree of circular polarization, vary significantly over the years (see also Maihara et al., 1976). Such variability has also been detected on shorter time scales by Serkowski (1969), who found that within four months the degree of linear polarization of VY CMa changed approximately 0.5%-point in V-band and 1%-point in B-band. Contrary to the degree of linear polarization, the angle of linear polarization seems to have remained relatively constant over the past 50 years. A possible explanation for these observations is that the overall asymmetric structure in the inner region around VY CMa is quite stable with time (resulting in a more or less constant χ), but that the distribution of scattering material located at even smaller separations from the star exhibits significant variations (causing changes in P_L). Such variations of the innermost scattering material could indicate recent ejections of dust from the star.

6.7.2 Spatially resolved polarization of nebula

The images of the total intensity and linearly polarized intensity of VY CMa in H-band are shown in Fig. 6.4. From IRDIS H-band data taken under similar atmospheric conditions (see Chapter 5), we estimate that our images have a spatial resolution (i.e., a full width at half maximum of the PSF) of ~47 mas, making them the highest-resolution NIR images of VY CMa to date. In the linearly polarized intensity image (Fig. 6.4, right), the asymmetric nebula of VY CMa is clearly visible and many of the well-known features can be discerned (see e.g., Monnier et al., 1999; Smith et al., 2001; Humphreys et al., 2007; Shenoy et al., 2013). To the south of the star, we distinguish the SW clump and the adjacent south knot (both at ~1.3″ from the star), the south arc (2.3″), and the bow-shaped feature known as arc 2 (4.3″). To the west of the star we discern the elongated arc-like feature known as the curved nebulous tail or northwest arc (2.5–4.4″) as well as part of the west arc (2.0″) located between this feature and the SW clump. We also detect the radially oriented northwest knot (0.6″) in the inner structure and the ridge connecting the SW clump and the inner structure. Due to the high spatial resolution, our linearly polarized intensity image shows the substructures within most of these features and reveals so-far-unresolved radial plumes of ejecta (similar to the northwest knot) in the inner structure. We also detect a relatively small and faint bow-shaped feature 1.2″ to the east of the star that has not been previously observed. Finally, we note that most of the observed features are so bright that they are also visible in the total-intensity image (see Fig. 6.4, left), even though this image is strongly contaminated by the ring of the adaptive-optics residuals and the diffraction pattern of the M2 support structure.

In addition to the linearly polarized intensity, Fig. 6.4 (right) displays the angle of linear polarization in the nebula of VY CMa. The angle of linear polarization largely follows a centrosymmetric pattern of azimuthal polarization, in agreement with the polarization maps of VY CMa at visible and NIR wavelengths from Jones et al. (2007), Shenoy et al.

(2015), and Scicluna et al. (2015). The pattern of azimuthal polarization can also be deduced from the Q_ϕ- and U_ϕ-images (see Fig. 6.8, bottom) which show most of the flux as positive Q_ϕ-signal. The predominantly azimuthal polarization is indicative of single scattering of the light from the central star and shows that most scattering material is optically thin in H-band.

Figure 6.4 (right) shows that the angle of linear polarization in the inner structure is not azimuthal everywhere. From the U_ϕ-image (see Fig. 6.8, bottom right), it follows that not only the inner structure, but also the SW clump exhibits non-azimuthal linear polarization. However, these U_ϕ-signals are probably artifacts of the finite-sized PSF (see Heikamp & Keller, 2019). In addition, at the smallest separations from the star the measurements may be affected by the spurious signals described in Sect. 6.6.2. Nevertheless, part of the U_ϕ-signals could be due to real non-azimuthal polarization, which would indicate that the circumstellar material in these regions is optically thick in H-band (as already found for the SW clump by Shenoy et al. (2013) and Shenoy et al. (2015)) and therefore scatters part of the light multiple times (see e.g., Canovas et al., 2015). From the region indicated with the dashed lines in Fig. 6.3, and following the same methods as used to determine the stellar polarization and its uncertainty (see Sects. 6.5 and 6.7.1), we find that the SW clump has an integrated degree and angle of linear polarization of $P_\mathrm{L} = 38.5 \pm 0.2\%$ and $\chi = 125.9 \pm 0.1^\circ$ in H-band. Because the degree of linear polarization is relatively large, any depolarization due to multiple scattering is most likely limited in the SW clump (Shenoy et al., 2015). Finally, we note that the images from Scicluna et al. (2015) show much stronger non-azimuthal polarization than Fig. 6.4 (right), but this is because the images from Scicluna et al. (2015) still contain the halo of polarized starlight. Indeed, the regions to the north and east of the star in these images have an angle of linear polarization of ~90°, close to the $\chi = 84.3 \pm 0.3^\circ$ we measured for the stellar polarization (see Sect. 6.7.1).

The final V-image of the central part around VY CMa in H-band as obtained from the reduction with a value of 173.4° for Δ_UT and Δ_M4 is shown in Fig. 6.7. In this image, we see relatively strong signals close to the star (in the inner structure), which, as discussed in Sect. 6.6.2, are most likely spurious in nature. Still, we cannot exclude the possibility that part of the signals are real incident V-signals. Figure 6.7 also shows signals at the position of the SW clump. These signals average to ~0%, which is as expected because we selected the value of Δ_UT and Δ_M4 used for this reduction under the assumption that there is no real incident V-signal in the SW clump (see Sect. 6.6.2). However, we are not certain about the exact value of Δ_UT and Δ_M4 and so the SW clump could in reality be circularly polarized. Using the same method as we used to determine the linear polarization of the SW clump, we find that for the data reductions with Δ_UT and Δ_M4 between 172.5° and 174.5° (the most likely range of values, see Sect. 6.6.2), the integrated normalized Stokes v in the SW clump lies between −1.0% and 1.2%. Overall, we cannot conclusively prove or disprove the presence of real incident V-signal in the spatially resolved parts of the nebula surrounding VY CMa. However, we can conclude that we do not detect the large circular-polarization signals on the order of 10% or more that are frequently found in star-forming regions and that result from magnetically aligned elongated dust grains (e.g., Bailey et al., 1998; Chrysostomou et al., 2000; Ménard et al., 2000; Buschermöhle et al., 2005; Kwon et al., 2013, 2014).

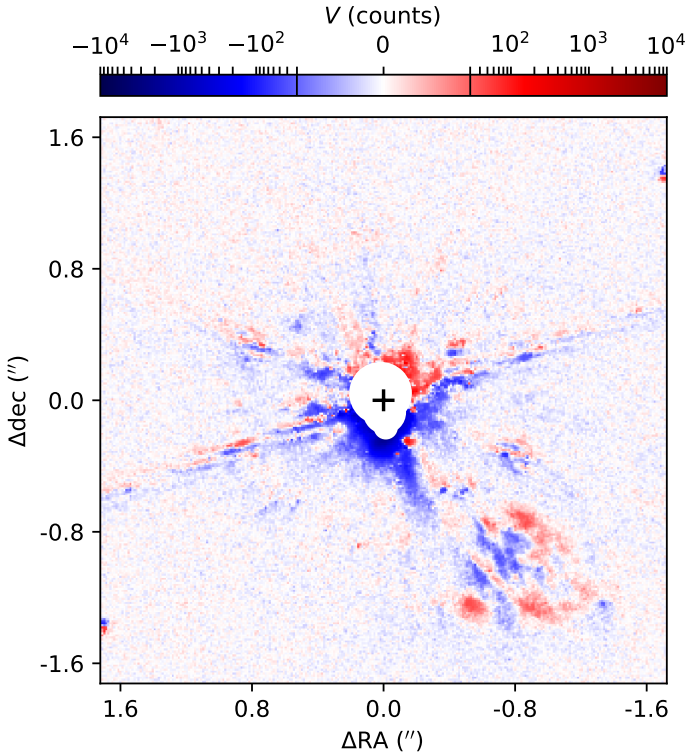

Figure 6.7: Central part of the image of Stokes V of VY CMa in H-band as obtained from the data reduction using a retardance of the UT and M4 equal to 173.4° and after subtracting the stellar polarization. Values smaller than -30 counts or larger than 30 counts are shown on a logarithmic scale, whereas values between -30 and 30 counts are shown on a linear scale. The position of the star is marked with the black plus sign. The white area around this plus sign masks the region that is obscured by the focal-plane mask of the coronagraph and that contains saturated pixels and pixels with values in the nonlinear regime of the detector.

6.8 Conclusions

We developed the observing scheme, data-reduction methods, and analysis tools to measure NIR circular polarization at sub-arcsecond resolution with SPHERE-IRDIS at the Very Large Telescope. We use SPHERE's image derotator, which acts as an almost perfect quarter-wave retarder in the H- and K_s-bands, as a polarization modulator to convert incident circular polarization into measurable linear polarization. We tested our observing scheme with linear- and circular-polarization measurements of the red hypergiant VY CMa and its asymmetric nebula in H-band. To reduce the observations, we adapted the IRDAP pipeline that uses the Mueller matrix model of Chapter 2 to correct for instrumental polarization effects.

Using this Mueller matrix model, we investigated the instrumental polarization effects of circular-polarization measurements. For both the H- and K_s-bands, we find that the polarimetric measurement efficiency is close to 100%, that the IP is <0.1%, and that the polarimetric crosstalk from incident linear polarization can reach values of up to ~15%. However, the crosstalk can have an uncertainty of several percent due to uncertainties in $\Delta_{\rm UT}$ and $\Delta_{\rm M4}$, the retardances of the UT and M4. Such large uncertainties in the crosstalk can create large spurious signals in the images after the data reduction. We therefore reduced the test data of VY CMa using a series of values for both $\Delta_{\rm UT}$ and $\Delta_{\rm M4}$ to find the value that minimizes the spurious signals. Assuming that there is no real incident circular polarization in one of the brightest regions of the nebula (the SW clump), the most likely value of $\Delta_{\rm UT}$ and $\Delta_{\rm M4}$ in H-band is 173.4°.

With this new value of $\Delta_{\rm UT}$ and $\Delta_{\rm M4}$, we performed a final reduction of the measurements of VY CMa. We find that the light from the star is polarized with a degree and angle of linear polarization of 4.07 ± 0.05% and 84.3 ± 0.3°, respectively, and a degree of circular polarization of 0.14 ± 0.04% (right-handed) in H-band. These polarization signals most likely originate from a spatially unresolved, asymmetric circumstellar structure located close to the star that is optically thick or contains magnetically aligned dust grains. Variations of the stellar polarization over the past 50 years may indicate recent ejections of dust from the star. From the linearly polarized intensity image, we detect so-far-unresolved radial plumes of ejecta close to the star as well as a faint bow-shaped feature to the east. We also find that the SW clump and the structures close to the star exhibit non-azimuthal linear polarization. However, these non-azimuthal polarization signals are probably artifacts of the finite-sized PSF, although part of the signals could be real and indicate multiple scattering. Finally, due to the uncertainty in $\Delta_{\rm UT}$ and $\Delta_{\rm M4}$, we cannot conclusively prove or disprove the presence of circular polarization in the nebula.

To enable accurate measurements of circular polarization and improve the accuracy of the IRDAP pipeline, we need to determine the true value of $\Delta_{\rm UT}$ and $\Delta_{\rm M4}$. To this end, we plan to observe a large, bright, nearly face-on viewed circumstellar disk (e.g., TW Hya; van Boekel et al., 2017). For such a disk we only expect azimuthally oriented linear polarization and no circular polarization, so that any circular polarization we measure should originate from uncorrected polarimetric crosstalk. We then perform a series of data reductions in which we vary the value of both $\Delta_{\rm UT}$ and $\Delta_{\rm M4}$ and find the value for which the total amount of (positive and negative) circular polarization in the disk (i.e., $|v|^2$) is minimized. Ideally, we would repeat these measurements at different parallactic and altitude angles so that we can fit separate values for $\Delta_{\rm UT}$ and $\Delta_{\rm M4}$. An alternative strategy for determining $\Delta_{\rm UT}$ and $\Delta_{\rm M4}$ would be to perform linear- and circular-polarization measurements of the highly linearly polarized twilight sky, for which the angle of linear polarization can be easily predicted using a single-Rayleigh-scattering model (see e.g., Harrington et al., 2011; de Boer et al., 2014; Harrington et al., 2017).

We stress that any future measurements taken with our observing scheme should also include regular linear-polarization measurements to enable the correction of the polarimetric crosstalk in the final image of Stokes V. We recommend to perform multiple integrations for each individual measurement (i.e., NDIT > 1) so that the frames that are smeared after a change of image-position-angle offset can be discarded without losing all data of a HWP cycle. Finally, we could in principal create an observation template for

circular-polarization measurements in which the HWP is not inserted. However, this is not really necessary because the contribution of the HWP to the polarimetric efficiency, IP, and crosstalk is small and these effects are corrected for in the data reduction.

Our observing scheme enables the first high-contrast, high-spatial-resolution measurements of NIR circular polarization in protoplanetary disks and the nebulae around evolved stars. Circular-polarization measurements can yield strong constraints on the distribution of scattering material, scattering asymmetries, dust properties, and magnetic-field geometries in these systems, and could even shed light on the emergence of homochirality in biomolecules. We plan to observe multiple young stars with bright, complex disks to explore the range of circular-polarization signatures in protoplanetary disks. If these observations are successful, we could add high-quality quarter-wave plates to SPHERE and implement dedicated circular-polarimetric modes for SPHERE-IRDIS at NIR wavelengths and SPHERE-ZIMPOL at visible wavelengths.

6.A Additional figures

Figure 6.8 shows the final images of Q, U, Q_ϕ, and U_ϕ of VY CMa in H-band after subtracting the stellar polarization. In addition, Fig. 6.9 displays images of the ratio of circular polarization to linearly polarized intensity $V/PI_{\rm L}$ for reductions of the H-band data of VY CMa using retardances of both the UT and M4 ranging from 170.5° to 180°.

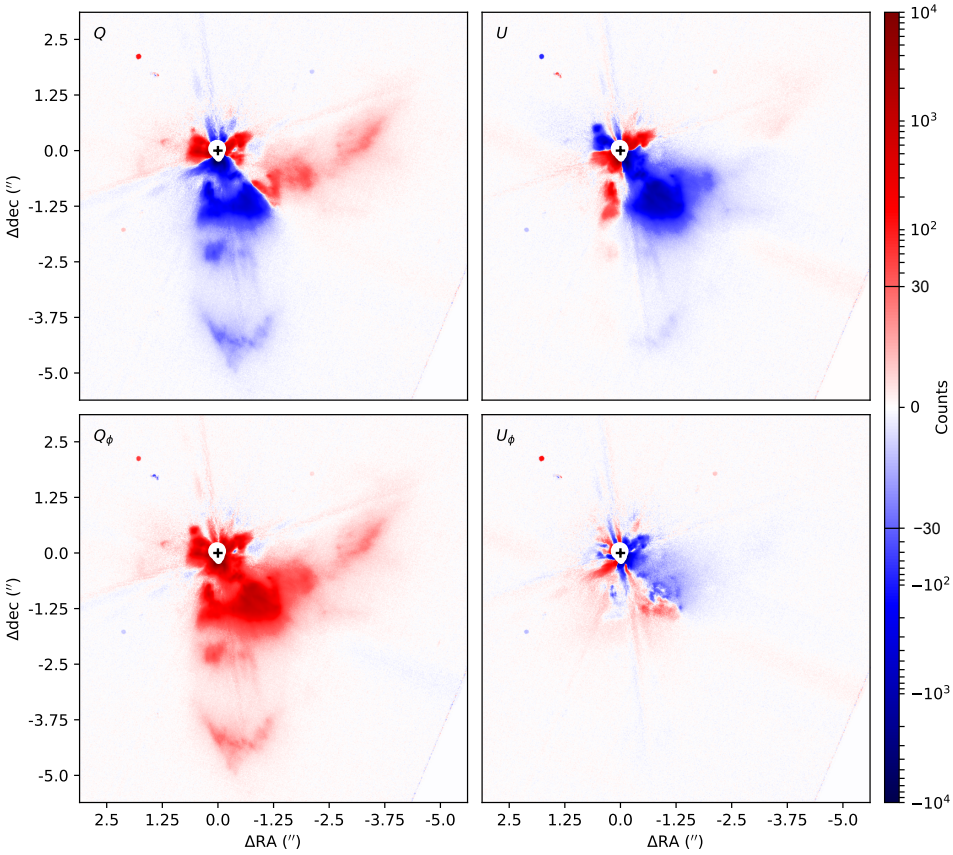

Figure 6.8: Images of Q (*top left*), U (*top right*), Q_ϕ (*bottom left*), and U_ϕ (*bottom right*) of VY CMa in H-band after subtracting the stellar polarization. In all images, values smaller than -30 counts or larger than 30 counts are shown on a logarithmic scale, whereas values between -30 and 30 counts are shown on a linear scale. The position of the star is marked with the black plus signs. The white areas around these plus signs mask the region that is obscured by the focal-plane mask of the coronagraph and that contains saturated pixels and pixels with values in the nonlinear regime of the detector.

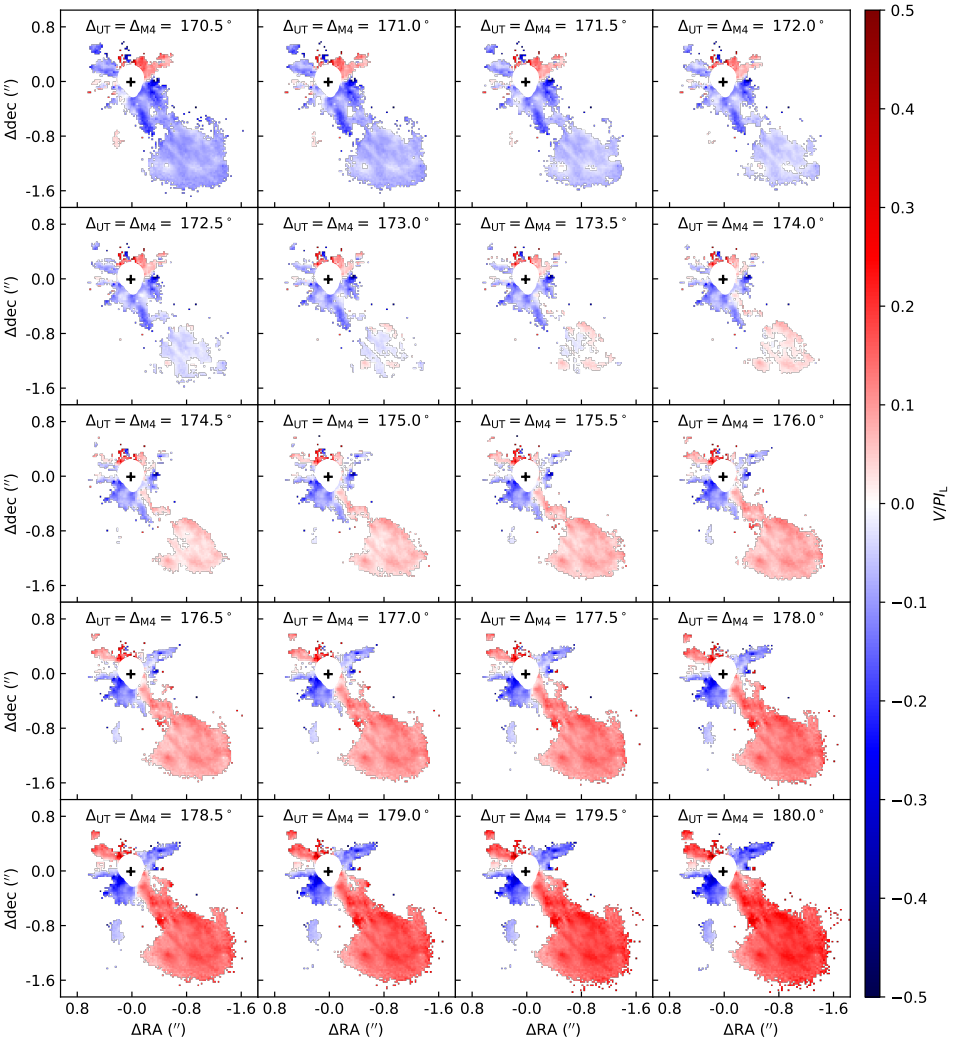

Figure 6.9: Images of the ratio of circular polarization to linearly polarized intensity V/PI_{L} for reductions of the H-band data of VY CMa using retardances of both the UT and M4 ranging from 170.5° to 180° in steps of 0.5°. The images show bins of 2×2 pixels for which both V and PI_{L} exceed 10 counts and for which $-0.5 \leq V/PI_{\mathrm{L}} \leq 0.5$. The position of the star is marked with the black plus signs. The white areas around these plus signs mask the region that is obscured by the focal-plane mask of the coronagraph and that contains saturated pixels and pixels with values in the nonlinear regime of the detector.

References

Avenhaus, H., Quanz, S. P., Garufi, A., et al. 2018, Astrophysical Journal, 863, 44
Avnir, D. 2021, New Astronomy Review, 92, 101596
Bailer-Jones, C. A. L., Rybizki, J., Fouesneau, M., Mantelet, G., & Andrae, R. 2018, Astronomical Journal, 156, 58
Bailey, J., Chrysostomou, A., Hough, J. H., et al. 1998, Science, 281, 672
Bastien, P., & Ménard, F. 1990, Astrophysical Journal, 364, 232
Beuzit, J. L., Vigan, A., Mouillet, D., et al. 2019, Astronomy & Astrophysics, 631, A155
Bonner, W. A. 1991, Origins of Life and Evolution of the Biosphere, 21, 59
Buschermöhle, M., Whittet, D. C. B., Chrysostomou, A., et al. 2005, Astrophysical Journal, 624, 821
Canovas, H., Ménard, F., de Boer, J., et al. 2015, Astronomy & Astrophysics, 582, L7
Canovas, H., Rodenhuis, M., Jeffers, S. V., Min, M., & Keller, C. U. 2011, Astronomy & Astrophysics, 531, A102
Cantalloube, F., Dohlen, K., Milli, J., Brandner, W., & Vigan, A. 2019, arXiv preprint arXiv:1907.03624
Carbillet, M., Bendjoya, P., Abe, L., et al. 2011, Experimental Astronomy, 30, 39
Chrysostomou, A., Gledhill, T. M., Ménard, F., et al. 2000, Monthly Notices of the Royal Astronomical Society, 312, 103
Chrysostomou, A., Menard, F., Gledhill, T. M., et al. 1997, Monthly Notices of the Royal Astronomical Society, 285, 750
de Boer, J., Girard, J. H., Mawet, D., et al. 2014, in Society of Photo-Optical Instrumentation Engineers (SPIE) Conference Series, Vol. 9147, Ground-based and Airborne Instrumentation for Astronomy V, 914787
de Boer, J., Langlois, M., van Holstein, R. G., et al. 2020, Astronomy & Astrophysics, 633, A63
Dohlen, K., Langlois, M., Saisse, M., et al. 2008, in Society of Photo-Optical Instrumentation Engineers (SPIE) Conference Series, Vol. 7014, Proceedings of the SPIE, 70143L
Garufi, A., Benisty, M., Stolker, T., et al. 2017, The Messenger, 169, 32
Gehrels, T. 1972, Astrophysical Journal Letters, 173, L23
Ginski, C., Benisty, M., van Holstein, R. G., et al. 2018, Astronomy & Astrophysics, 616, A79
Gledhill, T. M., & McCall, A. 2000, Monthly Notices of the Royal Astronomical Society, 314, 123
Guerri, G., Daban, J.-B., Robbe-Dubois, S., et al. 2011, Experimental Astronomy, 30, 59
Harrington, D. M., Kuhn, J. R., & Ariste, A. L. 2017, Journal of Astronomical Telescopes, Instruments, and Systems, 3, 018001
Harrington, D. M., Kuhn, J. R., & Hall, S. 2011, Publications of the Astronomical Society of the Pacific, 123, 799
Heikamp, S., & Keller, C. 2019, Astronomy & Astrophysics, 627, A156
Hough, J. 2006, Astronomy and Geophysics, 47, 3.31
Humphreys, R. M., Helton, L. A., & Jones, T. J. 2007, Astronomical Journal, 133, 2716
Jones, T. J., Humphreys, R. M., Helton, L. A., Gui, C., & Huang, X. 2007, Astronomical Journal, 133, 2730
Klare, G., Neckel, T., & Schnur, G. 1972, Astronomy & Astrophysics Supplement, 5, 239
Kwon, J., Tamura, M., Lucas, P. W., et al. 2013, Astrophysical Journal Letters, 765, L6
Kwon, J., Tamura, M., Hough, J. H., et al. 2014, Astrophysical Journal Letters, 795, L16
Kwon, J., Nakagawa, T., Tamura, M., et al. 2018, Astronomical Journal, 156, 1
Lucas, P. W., Hough, J. H., Bailey, J., et al. 2005, Origins of Life and Evolution of the Biosphere, 35, 29

Maihara, T., Noguchi, K., Oishi, M., Okuda, H., & Sato, S. 1976, Nature, 259, 465
Mathewson, A., & Myers, H. 1971, Physica Scripta, 4, 291
McPeak, K. M., Jayanti, S. V., Kress, S. J., et al. 2015, ACS photonics, 2, 326
Ménard, F., Chrysostomou, A., Gledhill, T., Hough, J. H., & Bailey, J. 2000, in Astronomical Society of the Pacific Conference Series, Vol. 213, Bioastronomy 99, ed. G. Lemarchand & K. Meech, 355
Modica, P., Meinert, C., de Marcellus, P., et al. 2014, Astrophysical Journal, 788, 79
Monnier, J. D., Tuthill, P. G., Lopez, B., et al. 1999, Astrophysical Journal, 512, 351
Nelson, D. L., Lehninger, A. L., & Cox, M. M. 2008, Lehninger principles of biochemistry (Macmillan)
O'Gorman, E., Vlemmings, W., Richards, A. M. S., et al. 2015, Astronomy & Astrophysics, 573, L1
Ordal, M. A., Bell, R. J., Alexander, R. W., Newquist, L. A., & Querry, M. R. 1988, Applied optics, 27, 1203
Patty, C. L., ten Kate, I. L., Sparks, W. B., & Snik, F. 2018, in Chiral Analysis (Second Edition), second edition edn., ed. P. L. Polavarapu (Elsevier), 29–69
Rakić, A. D. 1995, Applied optics, 34, 4755
Rakić, A. D., Djurišić, A. B., Elazar, J. M., & Majewski, M. L. 1998, Applied Optics, 37, 5271
Scicluna, P., Siebenmorgen, R., Wesson, R., et al. 2015, Astronomy & Astrophysics, 584, L10
Serkowski, K. 1969, Astrophysical Journal Letters, 158, L107
—. 1973, Astrophysical Journal Letters, 179, L101
Serkowski, K., Mathewson, D. S., & Ford, V. L. 1975, Astrophysical Journal, 196, 261
Shafter, A., & Jura, M. 1980, Astronomical Journal, 85, 1513
Shenoy, D. P., Jones, T. J., Packham, C., & Lopez-Rodriguez, E. 2015, Astronomical Journal, 150, 15
Shenoy, D. P., Jones, T. J., Humphreys, R. M., et al. 2013, Astronomical Journal, 146, 90
Smith, N., Hinkle, K. H., & Ryde, N. 2009, Astronomical Journal, 137, 3558
Smith, N., Humphreys, R. M., Davidson, K., et al. 2001, Astronomical Journal, 121, 1111
Takami, H., Shiba, H., Sato, S., Yamashita, T., & Kobayashi, Y. 1992, Publications of the Astronomical Society of the Pacific, 104, 949
van Boekel, R., Henning, T., Menu, J., et al. 2017, Astrophysical Journal, 837, 132
van Harten, G., Snik, F., & Keller, C. 2009, Publications of the Astronomical Society of the Pacific, 121, 377
Whittet, D. C. B., Martin, P. G., Hough, J. H., et al. 1992, Astrophysical Journal, 386, 562
Wittkowski, M., Hauschildt, P. H., Arroyo-Torres, B., & Marcaide, J. M. 2012, Astronomy & Astrophysics, 540, L12
Zhang, B., Reid, M. J., Menten, K. M., & Zheng, X. W. 2012, Astrophysical Journal, 744, 23